Electronic Theses and Dissertations, 2004-2019

2006

Characterization Of Microstructural And Chemical Features In Cu-in-ga-se-s-based Thin-film Solar Cells

Ankush Halbe
University of Central Florida

STARS Citation

CHARACTERIZATION OF MICROSTRUCTURAL AND CHEMICAL FEATURES IN Cu-In-Ga-Se-S-BASED THIN-FILM SOLAR CELLS

by

ANKUSH R HALBE
B.E. University of Pune, India, 2004

A thesis submitted in partial fulfillment of the requirements
for the degree of Master in Science
in the Department of Mechanical, Materials and Aerospace Engineering
in the College of Engineering and Computer Science
at the University of Central Florida
Orlando, Florida

Spring Term
2006

ABSTRACT

Thin-film solar cells are potentially low-cost devices to convert sunlight into electricity. Improvements in the conversion efficiencies of these cells reduce material utilization cost and make it commercially viable. Solar cells from the *Thin-Film Physics Group, ETH Zurich, Switzerland* and the *Florida Solar Energy Center (FSEC), UCF* were characterized for defects and other microstructural features within the thin-film structure and at the interfaces using transmission electron microscopy (TEM). The present thesis aims to provide a feedback to these groups on their deposition processes to understand the correlations between processing, resulting microstructures, and the conversion efficiencies of these devices. Also, an optical equipment measuring photocurrents from a solar cell was developed for the identification of defect-prone regions of a thin-film solar cell.

The focused ion beam (FIB) technique was used to prepare TEM samples. Bright-field TEM along with scanning transmission electron microscopy (STEM) and energy dispersive X-ray spectroscopy (EDS) including elemental distribution line scans and maps were extensively used for characterizing the absorber layer and interfaces both above and below the absorber layer. Energy-filtered transmission electron microscopy (EFTEM) was applied in cases where EDS results were inconclusive due to the overlap of X-ray energies of certain elements, especially molybdenum and sulfur.

Samples from *ETH Zurich* were characterized for changes in the CIGS (Cu(In,Ga)Se$_2$) microstructure due to sodium incorporation from soda-lime glass or from a post-deposition

treatment with NaF as a function of CIGS deposition temperature. The CIGS-CdS interface becomes smoother and the small columnar CIGS grains close to the Mo back contact disappear with increasing CIGS deposition temperature. At 773 K the two sodium incorporation routes result in large differences in the microstructures with a significantly larger grain size for the samples after post-deposition Na incorporation.

Porosity was observed in the absorber layer close to the back contact in the samples from *FSEC*. The reason for porosity could be materials evaporation in the gallium beam of the FIB or a processing effect. The porosity certainly indicates heterogeneities of the composition of the absorber layer near the back contact. A Mo-Se rich layer (possibly $MoSe_2$) was formed at the interface between CIGS/CIGSS and Mo improving the quality of the junction. Other chemical heterogeneities include un-sulfurized Cu-Ga deposits, residual Se from the selenization/ sulfurization chamber in $CIGS_2$ and the formation of Cu-rich regions which are attributed to decomposition effects in the Ga beam of the FIB. Wavy absorber surfaces were observed for some of the cells with occasional discontinuities in the metal grids. The 50 nm thick CdS layer, however, remained continuous in all the samples under investigation.

For a sample with a transparent back contact, a 10 nm Mo layer was deposited on ITO (indium tin oxide) before deposition of the $CIGS_2$ ($Cu(In,Ga)S_2$) layer. EFTEM maps indicate that a MoS_2 layer does not form for such a Mo/MoS_2-ITO back contact. Instead, absorber layer material diffuses through the thin Mo layer onto the ITO forming two layers of $CIGS_2$ on either side of Mo with different compositions.

Furthermore, an optical beam induced current (OBIC) system with micron level resolution was successfully developed and preliminary photocurrent maps were acquired to microscopically

identify regions within a thin-film solar cell with undesirable microstructural features. Such a system, when fully operational, will provide the means for the identification of special regions from where samples for TEM analysis can be obtained using the FIB technique to study specifically the defects responsible for local variations in solar cell properties.

ACKNOWLEDGEMENTS

TABLE OF CONTENTS

LIST OF FIGURES

LIST OF TABLES

LIST OF ABBREVIATIONS

BF	Bright field
CBD	Chemical Bath Deposition
CIGS	$Cu(In,Ga)Se_2$
$CIGS_2$	$Cu(In,Ga)S_2$
CIGSS	$Cu(In,Ga)SeS$
CTEM	Conventional Transmission Electron Microscopy
DF	Dark Field
EBIC	Electron Beam Induced Current
EDS	Energy Dispersive Spectroscopy
EELS	Electron Energy Loss Spectroscopy
EFTEM	Energy-Filtered Transmission Electron Microscopy
FIB	Focused Ion Beam
HAADF	High-Angle Annular Dark Field
HRTEM	High-Resolution Transmission Electron Microscopy
ITO	Indium Tin Oxide
LBIC	Light/Laser Beam Induced Current
OBIC	Optical Beam Induced Current
PDT	Post Deposition Treatment
PV	Photovoltaic
SAED	Selected Area Electron Diffraction
SLG	Soda Lime Glass

STEM	Scanning Transmission Electron Microscopy
TCO	Transparent Conducting Oxide
TEM	Transmission Electron Microscopy

CHAPTER 1. INTRODUCTION

1.1. Need for renewable energy

Energy sources can be classified as renewable and non-renewable. Today, most of the energy is generated by burning fossil fuels (coal, oil, natural gas) and other non-renewable sources. There is a growing worldwide demand for energy, while the exhaustion of the conventional energy resources is only a question of time. In addition, burning fossil fuels releases greenhouse gases into the atmosphere, while nuclear energy poses environmental problems related to large-scale consequences of reactor accidents (e.g., 20 years ago on April 26, 1986 in Chernobyl) and the storage or disposal of nuclear waste. For a growing energy demand in the growth of the global economy, mankind needs renewable sources of energy. Solar energy is the earth's major renewable energy resource; therefore, the exploitation of the energy from the sun is the potential key to a sustainable energy production in future. Conversion of sunlight into electricity using photovoltaic cells emits essentially no toxic or greenhouse gases, it requires no moving parts and does not produce noise, while the material requirements are extremely low. Only production and disposal/recycling of devices are critical in their effects on the environment. Photovoltaic systems can be installed in principle in every region of the earth. Some of the drawbacks of the PV technology include [1]:

(i) the intermittence and seasonality of sunlight, which is related to the lack of inexpensive and efficient methods to store electrical energy,

(ii) its cost, although prices for photovoltaic modules are dropping, and a fair cost evaluation including indirect costs and governmental subsidies is seldom taken into account, and

(iii) "ignorance".

1.2. Evolution of solar cells

A solar cell is a device which converts sunlight into electricity. The discovery of the photovoltaic effect by the French experimental physicist Alexandre Edmond Becquerel in 1839 set the stage for the research and development of solar cells. He found that the current between two metal plates immersed into hydrochloric acid shows a higher value when these plates are exposed to outdoor sunlight than if they are kept in the laboratory. It took more than hundred years to manufacture the first 'modern' solar cell which was based on single-crystalline Si with a diffused p-n junction having efficiencies close to 6% [2]. This was accomplished in 1954 at the Bell Laboratories, USA. The devices were referred to as 'solar batteries' in those days and were used as power supplies for rural telephone lines by the Bell Telephone system company in Georgia, USA, substituting regular batteries.

Single crystalline and polycrystalline solar cells currently available in the market are mostly silicon-based solar cells reaching efficiencies close to 25% for single crystalline Si [3]. Crystalline Si cells are reliable, efficient and environmentally compatible devices, but they absorb sunlight relatively poorly and hence require large thicknesses (upto 250 μm [1]) to reach reasonable conversion efficiencies.

1.3. Introduction to thin-film solar cells

Thin-film solar cells were developed from the 1970s, with the original aim to achieve a better power-to-weight ratio for space applications. Today, the driving force for development of thin-film solar cells is mainly their potential to reduce manufacturing costs and material utilization. The earliest thin-film cells were based on Cu_2S/CdS and suffered from poor stability owing to the high diffusivity of Cu. Amorphous hydrogenated silicon (a-Si:H) cells entered the PV market in the 1980s and today are increasingly challenged by CdTe- and $Cu(In,Ga)Se_2$-based cells. One of the problems with thin-film materials other than a-Si:H is that they are not used elsewhere in the electronics industry. Therefore, there is comparatively little expertise about them [1]. Presently, the most efficient single junction thin-film solar cells are made from $Cu(In,Ga)Se_2$ (CIGS) and CdTe absorber layers corresponding to efficiencies as much as 19.5% [4] and 16.5% [5] respectively. The possibility for the use of $Cu(In,Ga)S_2$ ($CIGS_2$) and $Cu(In,Ga)(Se,S)_2$ (CIGSS) as absorber layer materials have also been explored [6].

Among the advantages of CIGS and CdTe cells over single-crystal Si cells is that sunlight is absorbed much more efficiently in these compounds and hence absorber thicknesses of a few micrometers are sufficient to absorb most of the useful part of the sunlight. Solar cells are small-area devices. Since the electrical current delivered by a solar cell depends on the illuminated area, the cell cannot be made arbitrarily large without suffering severe current losses due to the limited conductivity of the transparent conducting front contact. Therefore, individual small-area cells must be connected in series, which results in a large-area device (the solar "module") that delivers comparatively high voltages and low currents [7].

1.4. Components of thin-film solar cells in the present study
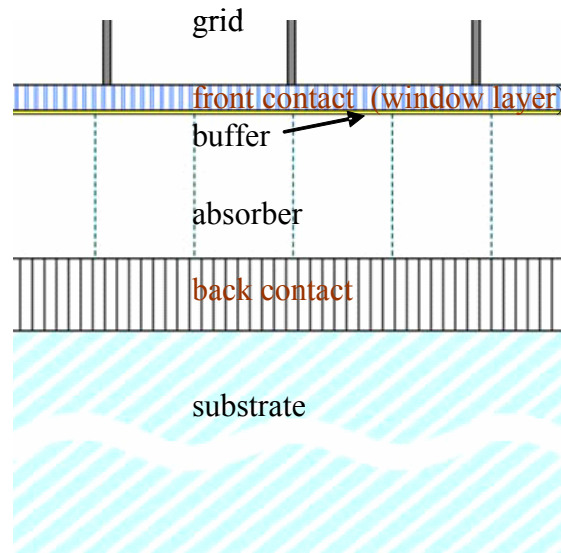
Figure 1. Device structure of a typical thin-film substrate solar cell.

1.4.1. Substrate

The substrate is a passive component in the device and is required to be mechanically stable, matching the thermal expansion coefficients with the other deposited layers and being chemically inert during the device fabrication. Thin-film solar cell devices are configured in either substrate or a superstrate configuration. For the superstrate configuration, the substrate is transparent and the contact is made by a conducting oxide coating on the substrate. For the substrate configuration, the most common choice of substrate is glass. The use of flexible substrates, like stainless steel foils/polymer films, ceramics, etc has also been explored in refs. [3] and [8].

Both superstrate and substrate device structures are currently being pursued for CIGS device fabrication. The substrate configuration appears to play an active role in improving the photovoltaic performance of the CIGS absorber materials by providing Na from the soda-lime

4

glass which improves grain growth and cell performance [9]. In the present thesis, thin-film solar cells with substrate configuration are studied.

1.4.2. Transparent conducting oxide (TCO) window layer

A 'window layer' consisting of a TCO forms the front contact of the cell. It is transparent to the incident photons and exhibits good electrical conductivity.

A ZnO bilayer is most often used for the transparent front contact in CIGS solar cells. The first layer is a thin intrinsic ZnO (i-ZnO) film to improve the band alignment and prevent shunting [10]. This layer is typically 50 nm thick, has high resistivity (compared with the second layer) and good transmissivity. The second layer is the actual front contact and consists of aluminum-doped ZnO (ZnO:Al). Thickness and material properties of the ZnO:Al layer are determined by a trade-off between transparency and conductivity. Other TCOs include SnO_2, In_2SnO_3 (ITO), etc. [11], [13]. RF magnetron sputtering is often used for the deposition of the front contact.

1.4.3. Front contact grid

For minimal optical losses in the window layer, a reduction of its thickness is desirable. On the other hand, a good conductivity is required in order to avoid resistive current losses. A good trade-off can be achieved when the current collection is supported by a metal grid deposited onto the front contact. Although the application of the grid is beneficial to the cell performance, it also contributes to the reduction of the active cell area.

Ni-Al grids are the most commonly used. A 50nm Ni layer is applied to reduce the formation of a resistive Al_2O_3 barrier followed by a 1 μm thick Al layer [14]. These layers are typically

deposited by electron-beam evaporation with aperture masks. Cr-Ag grids have also been used in certain cases [6].

1.4.4. P-type absorber layer

This is the most important layer in a thin-film solar cell where photons (having energies larger than the band-gap energy of the absorber) are converted into electron-hole pairs. This is essentially a p-type semiconducting layer having a thickness of 2-3μm.

The absorber layers studied in the present thesis include CIGS, CIGS$_2$ and CIGSS. Some of the successful methods for the deposition of the above absorber layers include co-evaporation (of constituent elements) [15] and DC magnetron sputtering of alloy targets [6] (Cu-Ga, In) with selenization (for CIGS) or sulfurization (for CIGS$_2$) of the deposited precursors. Naturally, deposition of such complex compounds can only be achieved by accurately controlling the deposition parameters. The band gap of the absorber is primarily influenced by the In/Ga concentration ratio and also by the Cu content. Such "band-gap engineering" [16] is often exploited in high efficiency solar cells which show varying In/Ga concentration ratios.

1.4.5. N-type buffer layer

The primary function of a buffer layer in a heterojunction solar cell is to form an n-type junction with the p-type absorber layer while admitting a maximum amount of light to the junction region and absorber layer; no photocurrent generation occurs in the buffer layer. The term 'buffer' layer refers to the role of this layer as an adjusting element between absorber and the window layer thus reducing lattice mismatch, affecting interdiffusion processes and adjusting the valence and

conduction bands between these two layers [17], [18]. The buffer layer also helps to protect the absorber layer from ion damage during the bi-layer window sputtering.

The CIGS/ CIGS$_2$/ CIGSS thin-film solar cells typically use a 50 nm CdS buffer, which is deposited by chemical bath deposition (CBD) technique. However, the use of CdS as an n-type buffer layer has a few drawbacks. The band-gap of CdS is low (2.4 eV) [19], such that significant amounts of photons are absorbed by the CdS layer before reaching the absorber. Furthermore, the toxicity of Cd raises environmental issues.

1.4.6. Back contact

The back contact is deposited on the glass substrate and is ohmic in nature. Mo is the most common choice for the back contact since it does not diffuse into the absorber layer and forms a low-resistivity contact with the absorber. However, Mo easily oxidizes [20] and this water-soluble oxide leads to long-term degradation of the solar cell performance Also, the reflectivity of Mo is low. This could be a drawback when using thin absorbers (less than 2 μm) since not all the photons having energies greater than the band-gap can be absorbed in a single pass through the absorber [21].

Recent studies have shown that the contact between Mo and the absorber is ohmic probably due to the formation of MoSe$_2$ /MoS$_2$ at the interface between CIGS/CIGS$_2$ /CIGSS absorbers and Mo [22]. The advantage of using MoSe$_2$ /MoS$_2$ layers as a buffer layer between Mo and the absorber has been exploited by developing these layers intentionally on a TCO back contact (usually ITO) [12].

1.5. Deposition parameters for the thin-film solar cells under study

The thin-film solar cells used for characterization in the present thesis were obtained from two sources namely the *Thin-Film Physics Group, ETH Zurich*, Switzerland and the *Florida Solar Energy Center (FSEC)*, Cocoa, Fl.

The solar cells from ETH Zurich comprised of CIGS absorber layers. To study the effects of Na on CIGS, certain Na incorporation strategies were devised. If soda lime glass is used as substrate, sodium can diffuse through the Mo back contact. A viable alternative for Na incorporation in CIGS layers on Na free substrates is the deposition of Na-compounds before, during or after deposition of the CIGS layer [23]. Thus, there were 2 sets of samples. In the first set, Na diffusion from soda lime glass (SLG) was studied. The second set of samples was studied after a NaF post deposition treatment (PDT). To avoid the interference of Na from SLG, an Al_2O_3 diffusion barrier was deposited in the second set between the back contact and the SLG.

A three stage [24] process was used for the preparation of the CIGS absorber layers with temperatures for CIGS deposition are as indicated in table 1. Immediately after cooling down the samples, NaF was deposited in-situ for the sample with Al_2O_3 diffusion barrier. The other set of samples was not treated with NaF. The cells were completed by deposition of CdS, i-ZnO, ZnO:Al, and Ni/Al. Each pair of samples (i.e. with and without Al_2O_3 diffusion barrier at the same temperature) was processed together, such that the only difference in the deposition process was the deposition of the Al_2O_3-diffusion barrier and the exposure to NaF vapor.

Table 1. Deposition sequence and temperatures of CIGS-based thin-film cells developed by the *Thin-film Physics Group, ETH Zurich,* Switzerland

Stages	Depositions	Temperature			
		Sample set 1	Sample set 2	Sample set 3	Sample set 4
1st stage	$(In,Ga)_xSe_y$ precursor	643K	673K	673K	673K
2nd stage	Cu-Se co-deposition	643K	673K	773K	853K
3rd stage	In, Ga, Se addition	643K	673K	773K	853K
	Annealing for 20 minutes	643K	673K	673K	673K

The samples obtained from FSEC comprised of CIGS, $CIGS_2$ and CIGSS absorber layers. The basic device configuration is as shown in table 2.

Table 2. Device configuration of thin-film solar cells developed at *FSEC*, Fl, USA

	Sample set 1	Sample set 2	Sample set 3
Substrate	Soda lime glass	Soda lime glass	Soda lime glass
Back contact	Mo	Mo or ITO- Mo/MoS$_2$	Mo
Absorber layer	CIGS	$CIGS_2$	CIGSS
Buffer layer	CdS	CdS	CdS
Front contact	i-ZnO, ZnO:Al	i-ZnO, ZnO:Al	i-ZnO, ZnO:Al
Front contact grid	Ni-Al or Cr-Ag	Ni-Al or Cr-Ag	Ni-Al or Cr-Ag

The absorber layers prepared at FSEC (table 2) were deposited by DC magnetron sputtering of the precursors in the following sequence: Cu-Ga, In, Cu-Ga. The precursors were then sulfurized with dilute H_2S and/or selenized depending on the type of absorber layer deposited. The ITO-Mo/MoS$_2$ back contact was developed by depositing 450 nm ITO, 10 nm Mo and the precursors on glass followed by sulfurization of the precursors to convert Mo into MoS$_2$.

1.6. Objectives of the present thesis

Thin-film solar cell technology is an answer to the depleting energy resources in the future. The biggest challenge being faced by the various groups around the world today is to improve the conversion efficiencies of these cells. The present thesis aims to provide a vital feedback to ETH Zurich and FSEC on their deposition processes and in-turn improve their solar cell efficiencies.

The thin-film solar cell system is very complex consisting of close to 10 elements which are not always in their regular positions but are interdiffusing across the interfaces and the grain boundaries. Many of the alloys formed during the deposition process show an inhomogeneous composition and a considerable density of impurities. TEM is a powerful tool for defect characterization of these thin-film structures. A high-resolution structural and chemical analysis of the various layers and interfaces helps in the identification of loopholes in the device processing. Some of the important issues discussed in the TEM study are as follows:

- Effect of Na incorporation on CIGS grain size and surface roughness

- Influence of rough CIGS surfaces on top layers

- Presence of porosity in the absorber layers with segregation along the pores

10

- Diffusion of $CIGS_2$ through Mo onto the TCO (ITO)

- Formation of $MoSe_2$ at the Mo-CIGS interface

- Other chemical heterogeneities

Besides TEM studies, equipment for the measurement of the optical-beam induced current (OBIC) has been developed to identify regions within a thin-film solar cell with detrimental microstructural features. Such a system would help to identify the regions from where the TEM samples can be prepared for further analysis. Though such a system is not fully operational yet, the objective of presenting it in the thesis is to prove the working principle of the system with some preliminary results.

The thesis is structured in the following way. Chapter 2 is a literature review on the characterization techniques employed for the analysis. Chapter 3 is the experimental work discussing the sample preparation details using the FIB, the different TEM imaging and chemical analysis techniques employed, and the setup and operation of the OBIC equipment. Chapter 4 discusses the results from TEM analysis and OBIC. Finally, the concluding remarks are expressed in chapter 5.

CHAPTER 2. CHARACTERIZATION TOOLS

2.1. Focused Ion Beam (FIB) technique

The Focused Ion Beam (FIB) technique is one of the methods of TEM sample preparation. A typical FIB instrument consists of a vacuum system, a liquid metal ion source, ion column, stage, detectors, gas inlets, and computer (figure 2a). It operates in a similar way as a scanning electron microscope, but instead of electrons gallium ions are focused on the sample.

A gallium reservoir is in contact with a sharp tungsten needle and wets its tip (figure 2b). A high extractor voltage (around 10 kV) induces a high electric field of more than 10^{10} V/m at the tip [25]. A sharp cone of Ga atoms forms at the tip and Ga atoms are ionized and emitted. Beam deflectors are used to scan the Ga beam across the sample. A highly magnified image is created as the beam scans the sample. This allows viewing of the required microstructural features. A secondary electron detector is typically used for imaging.

The probe current can be varied from a few ten pA to several nA. Material is removed at specific locations using beam diameters as small as 5 nm for the smallest probe current. While high probe currents are used to remove large quantities of material and to dig trenches of several μm in depth into the sample, the small probe currents are used as final preparation steps in TEM sample preparation. To protect the sample area of interest a Pt layer (figure 3a) is deposited in the FIB system. This is accomplished by a gas injection needle which is positioned close to this sample region. The organo-metallic precursor gas from the injection system decomposes in the Ga ion beam and Pt is deposited. After removing the gas injection needle, the cutting of a sample for

TEM starts. A five axis (X, Y, Z, tilt, rotate) motorized eucentric stage motion allows rapid sputtering at various angles to the specimen. Around the stripe with the protective Pt layer the sample is cut to a depth of a few μm.
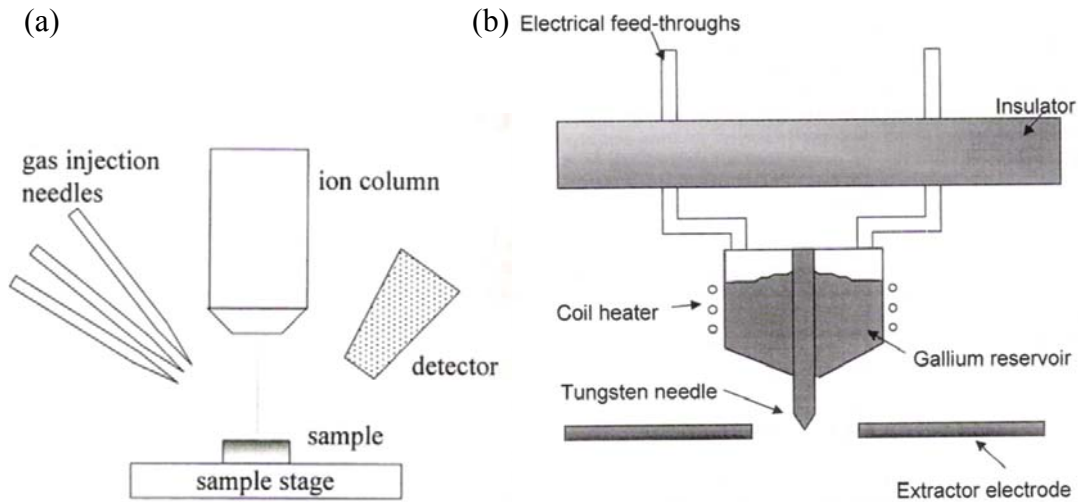
Figure 2. Schematic diagram of (a) a basic FIB system and (b) liquid metal ion source [25].

2.1.1. Ex-situ lift out of TEM samples

In this method, the Ga beam size is successively reduced and the sample is thinned down to below 1000 nm (figure 3b). After tilting the sample to 45° the cut section is viewed from the side and the bottom of the section is cut (figure 3c). Further thinning at both sides of the section is done with ion currents below 100 pA [25]. When a thickness between 50 to 100 nm is reached the sides of the section are cut off. The specimen is removed from the FIB system and placed under an optical microscope. A thin quartz needle attached to a micromanipulator is approached to the cut region. The thin section usually clings to the tip of the quartz needle due to electrostatic forces and can be removed from the specimen. In the next step, the quartz needle is approached to a fresh Cu grid with an amorphous carbon film. When the quartz needle is

touching the carbon film the thin sample section sticks typically easily to the carbon film. The thin section on the Cu grid is then ready for TEM analysis (figure 3d).
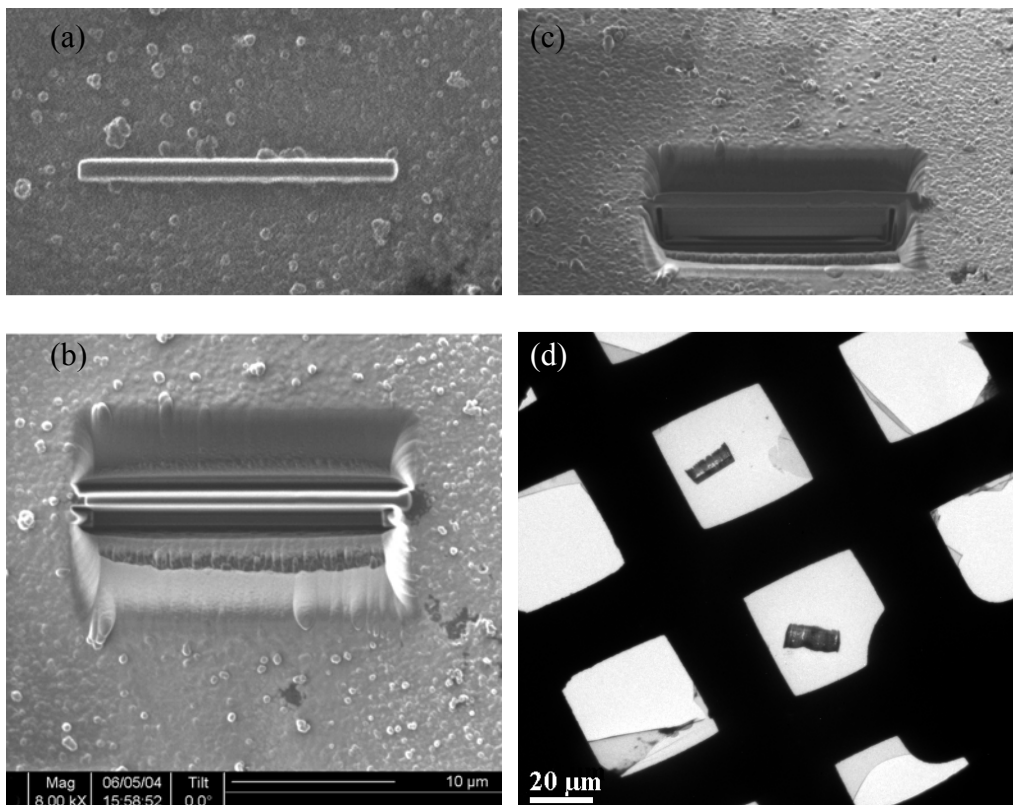
Figure 3. Different steps of an ex-situ lift out process. (a) Pt deposition, (b) cutting of the sides to form a thin section, (c) side view (at 45° tilt) of the section with the bottom cut, (d) low-magnification TEM images of sample sections deposited on a carbon film on a Cu grid.

2.2. An Introduction to Transmission Electron Microscopy

TEM is a very powerful tool for micro- and nanostructural characterization of materials using a beam of high-energy electrons to examine objects [26]. A TEM study can yield the following information about the material studied [27]–

14

1. Topography: The surface features and texture of a cross-sectional specimen.

2. Morphology: The size, shape and arrangement of the particles which make up the specimen as well as their relationship to each other on the scale of atomic diameters.

3. Crystallographic information: The arrangement of atoms in the specimen and their degree of order, detection of atomic-scale defects in areas a few nanometers in diameter.

4. Compositional information: The elements and compounds the sample is composed of and their relative ratios, in areas a few nanometers in diameter.

TEM is a two-dimensional imaging technique applied to three-dimensional systems. Thus, the interpretation of TEM micrographs and the chemical studies is not straightforward and becomes more complicated the higher the resolution is.

2.2.1. Components of a Transmission Electron Microscope

A transmission electron microscope consists of an electron source (electron gun), condenser lenses, an objective lens, imaging system (consisting of the diffraction lens, intermediate lenses, and projector lenses depending on the type of microscope), and a viewing screen (figures 4 a & 4b).

The *condenser lens system* with at least two lenses essentially demagnifies the electron probe thus reducing the area illuminated by the electron beam. A *condenser aperture* selects electrons near the optical axis for illumination of the sample.

The sample is centered within the upper and lower pole pieces of the objective lens (figure 4b). The upper part of the objective lens generates a parallel beam entering the sample. The lower part of the objective lens is used to generate a magnified image. Additionally, a diffraction pattern is formed in the back focal plane of the lens. An *objective aperture* is used in this back

focal plane (it's also called the diffraction plane as a diffraction pattern is formed there) to select one or more Bragg reflections and to form magnified images of the sample only with contributions from Bragg reflections transmitted through this aperture.

The lenses in the imaging system are used to obtain additional magnification of the sample image or of the diffraction pattern. In the plane of the first image (formed by the objective lens) of the sample a *selected area aperture* can be inserted, which allows only electrons from a limited area of the sample to go through. By different excitations of the intermediate lens either the imaging plane or the diffraction plane of the sample forms a magnified image on the viewing screen of the microscope.

For the *camera system* a fluorescent material like ZnS is used on a viewing screen. This screen can be tilted up to take micrographs on photographic films, on a CCD camera, on imaging plates, to use a TV-rate camera for imaging. Alternatively, electrons can also be brought on other detectors, like the bright-field (BF) and dark-field (DF) detectors or the high-angle annular dark-field (HAADF) detector in the scanning transmission mode (STEM), or the electron can be transferred to an electron energy loss spectrometer. In the scanning mode, a convergent small electron probe is scanned over the sample. Deflection coils are used to move the probe across the sample.
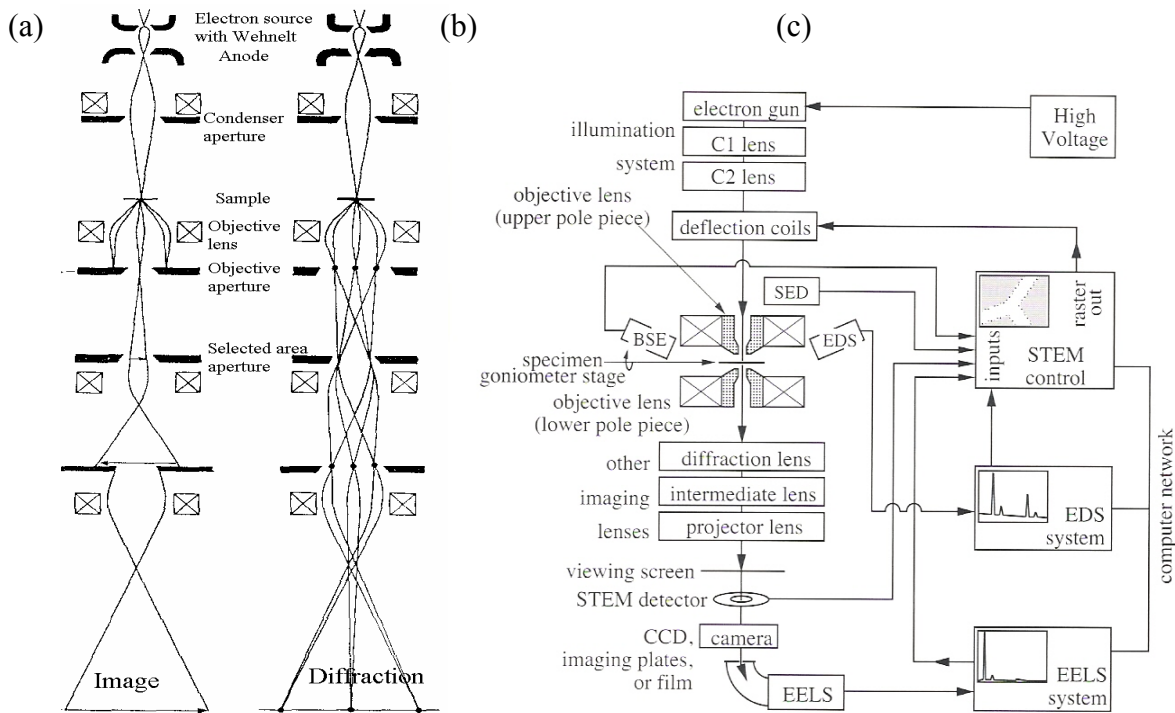
Figure 4. (a) Imaging and (b) diffraction mode of the transmission electron microscope dependent on the excitation of the intermediate lens, (c) Schematics of the electron microscope with system control and data acquisition [26].

The sample itself is mounted on a *sample holder* which is held by a *goniometer* in the gap between the upper and the lower pole piece of the objective lens. Double tilt holders allow for sample tilts in different directions.

2.2.2. Conventional Transmission Electron Microscopy (CTEM)

The conventional TEM mode uses a broad, nearly parallel electron beam with a diameter of several micrometers. Apertures in the back focal plane and in the image plane may be applied to increase the contrast or to select an area of interest.

2.2.2.1. Bright-field and dark-field TEM

These techniques essentially give a crystallographic contrast for polycrystalline samples such as CIGS/CIGS$_2$ solar cells. The contrast is obtained by the insertion of an objective aperture in the back focal plane of the objective lens.

When one of the apertures in this diaphragm is centered about a selected Bragg reflection in the diffraction pattern only this beam can contribute to the formation of an image. All other beams are blocked by this diaphragm. If the objective aperture is centered about the undiffracted beam, we have *bright-field* conditions (figure 5 a). Only the undiffracted beam or, for larger apertures, also a few of the low-indexed Bragg reflections are then contributing to the first image in the imaging plane of the objective lens. This way, the contrast in the micrograph is enhanced when compared to an image without an aperture. Using this technique, crystal defects can be identified, as they locally modify the *diffraction contrast*, i.e., how many electrons are scattered to other Bragg reflections and are lost to the undiffracted beam.

Electron beam

| Sample |
| Objective | lens |
Diffracted beams
Diffraction ↓ pattern
Objective diaphragm with objective aperture
Bright-field image of the sample

| Deflection | coil |
| Deflection | coil |
| Sample |
| Objective | lens |
Diffracted beam
Shifted diffraction pattern
Objective diaphragm with objective aperture
Dark-field image of the sample
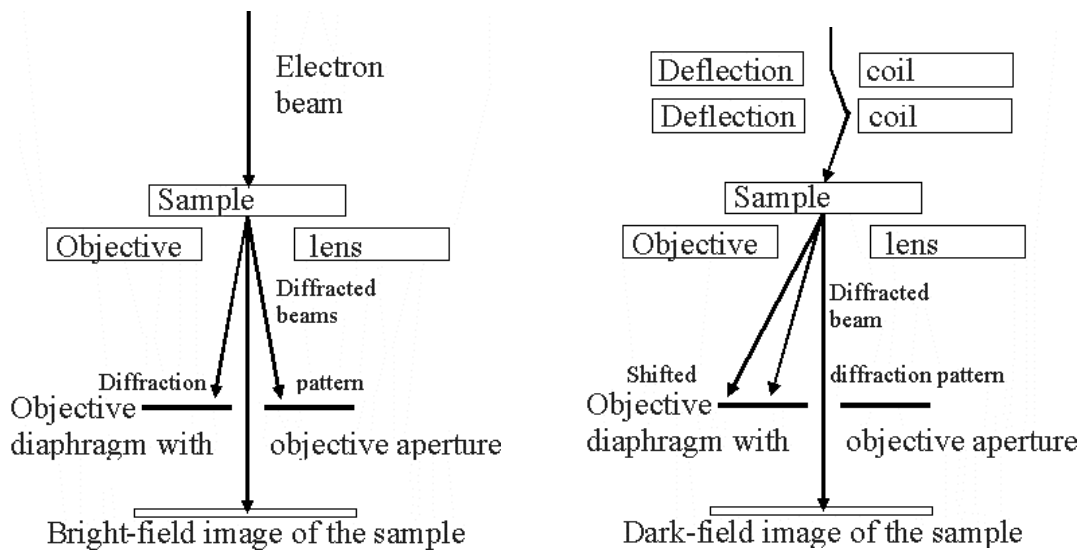
Figure 5. (a) Bright-field and (b) dark-field imaging techniques.

18

In *dark-field* imaging (figure 5b) the incident electron beam is tilted with respect to the optical axis of the objective lens. Therefore, the electron diffraction pattern in the back-focal plane is shifted. The electron beam is tilted in such a way, that one Bragg reflection is on the optical axis. The objective aperture is then centered around this Bragg reflection. All other reflections are excluded by the diaphragm and do not contribute to the image. In imaging mode only those regions appear bright which contribute to the Bragg reflection in the objective aperture. All other regions appear dark.

2.2.2.2. Selected-area electron diffraction (SAED)

As see in fig 4b, the diffraction pattern contains electrons from the whole area of the specimen that is illumined. Such a pattern is not very useful because the specimen will often be buckled. Furthermore, the direct beam is often so intense that it will damage the viewing screen. Insertion of an aperture in the image plane of the microscope results in the blocking of those electrons which fall outside the dimensions of the aperture. SAED is a useful tool to acquire electron diffraction patterns from a certain area of interest on the specimen.

2.2.3. High-resolution transmission electron microscopy (HRTEM)

The HRTEM technique uses phase contrast to image lattice fringes and atomic structures unlike the conventional TEM techniques which operate at low/medium magnification mode (upto 200,000 X) and employ mass-thickness or diffraction contrast. The imaging of the atomic lattice requires its orientation in such a way that the atomic columns of this lattice are oriented parallel to the incident electron beam. High-resolution micrographs of crystal lattices can be acquired in modern transmission electron microscopes with high lateral resolution better than 2 Å.

2.2.4. Analytical TEM using Scanning transmission electron microscopy (STEM)

The scanning TEM mode is different from the conventional TEM mode since it uses a convergent electron probe with a few angstroms in diameter. The probe scans the sample using a set of deflection coils. Such a highly convergent beam allows probing with a high degree of specificity.

Electrons impinging on a specimen induce emission of X-rays while they also lose their energy owing to the interaction with the electron shells of the atoms. These processes can be used to chemically analyze areas of interest. Additionally, electron beams diffracted by atomic planes of the specimen may be detected by an annular detector in order to image the specimen.

2.2.4.1. Image formation by a high-angle annular dark field detector (HAADF)
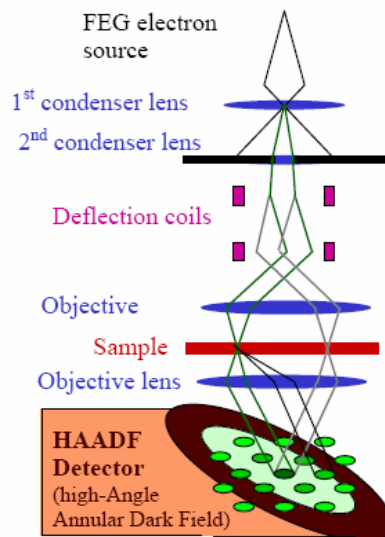
Figure 6. Arrangement for imaging in HAADF-STEM mode [28]

The high-angle annular dark field detector (figure 6) is an annular detector positioned above the projection lenses and has been developed for high-angle collection of electrons. The acceptance

angle can be changed by varying the camera length. At shorter camera lengths, the collection angle increases and elastically scattered electrons are detected. This results in a HAADF-STEM image with a Z-contrast due to the strong dependence of contrast on the atomic number. A STEM image is recorded on the detector as a function of position.

2.2.4.2. Energy Dispersive X-ray spectroscopy (EDS)

Electrons passing through the specimen interact with inner-shell electrons ejecting them as secondary electrons. These empty inner-shell states are subsequently occupied by other inner-shell electrons from higher energy levels. This results in an X-ray spectrum characteristic to the specific elements. Since a huge number of electrons impinge the specimen, a cascade of X-rays is emitted from the specimen and is detected by the X-ray detector.

A typical X-ray detector consists of Si(Li) or Ge single crystal with a Be window. Electron-hole pairs are generated when X-rays hit the detector area. The number of charges produced depends on the energy of the incoming X-ray. In an X-ray spectrum, the number of X-rays with a certain energy is plotted as a function of their X-ray energies.

The EDS detector is always situated above the specimen to minimize the background signal (e.g from bremsstrahlung X-rays generated in the forward direction) in the spectrum. The sample is typically tilted about 20° towards the detector to minimise absorption of low-energy X-rays within the sample (figure 7). Unfortunately, the X-rays and secondary electrons generated in the volume illuminated by the electron probe, can themselves excite atoms and cause the emission of additional X-rays. Sample regions not illuminated by the electron probe or even parts from the microscope can therefore contribute to the EDX spectrum. Therefore, special care has to be taken

in quantitative EDX analysis to account for a possible excitation of x-rays in neighbouring regions.
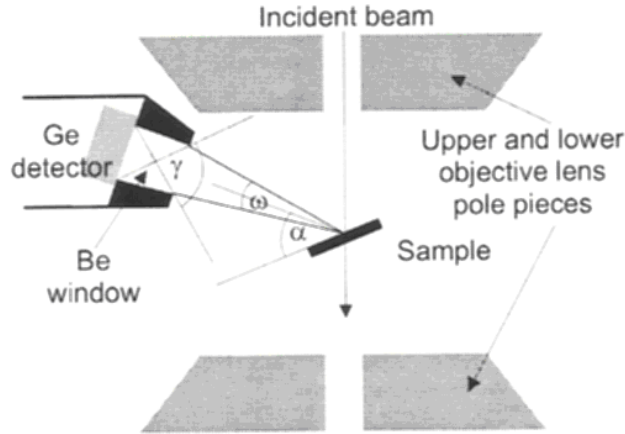
Figure 7. Sample geometry for analysis with an EDX detector [26]

EDS is well suited for the detection of heavy elements. Most of the elements in CIGS/CIGS$_2$ solar cells are heavy and hence EDS is an important tool in chemical analysis of the thin-film layers and to study the interdiffusional processes across the interfaces.

The EDX spectra can be obtained in the following formats –

1. Point measurements - These are essentially the spectra obtained by illuminating a very small area (down to 1 nm diameter with reasonable count rate is possible) of the sample.

2. Line scans – The small electron probe is sequentially positioned on points along a line. For each electron probe position and EDX spectrum is obtained.

3. Area scans/ maps – The small electron probe is sequentially positioned on points on a two-dimensional grid to form a map of the analyzed element.

Quantification of EDS data is a complicated task which requires the consideration of several issues [17] –

1.   Quantification of EDS data is always connected with the use of standards.

2.   Accuracy of quantification becomes worse with increasing number of elements.

3.   Since the STEM mode uses a probe as small as a few angstroms, the statistics of EDX measurements are poor.

4.   The quantification of lighter elements is more erroneous than the heavier ones since the probability of absorption of X-rays from light elements is always high.

5.   The number of counts should be as large as possible to guarantee favourable statistics.

6.   Absorption effects may influence the quantification considerably.

7.   Contamination of the sample during its preparation leads to erroneous results.

2.2.5. Electron energy loss spectroscopy (EELS)
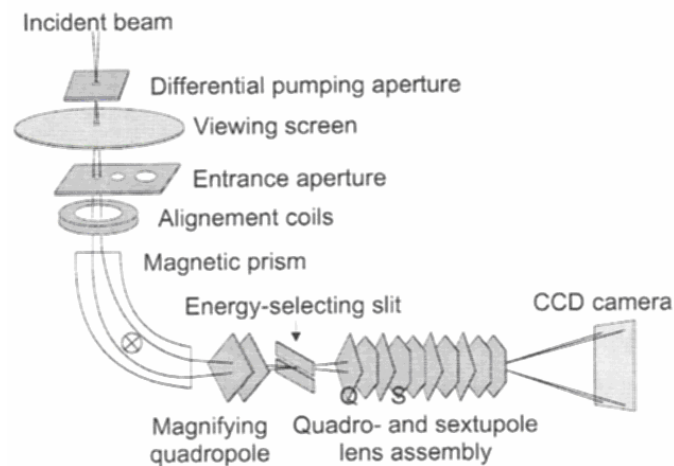
Figure 8. Principle of a post-column electron energy loss spectrometer with the option of energy-filtered imaging. [26]

The energy losses of electrons (after passing the sample) can be analyzed by electron energy-loss spectroscopy (EELS). If E_0 is the energy of the incident electron, E_b is the binding energy of the inner-shell electron and E_{kin} is the kinetic energy of the ejected inner-shell electron, the energy loss of incident electron ΔE, after interaction with the inner-shell electron can be written as-

$$\Delta E = E_0 - (E_b + E_{kin})$$

In a homogeneous magnetic field, electrons are forced on a circular trajectory with a radius according to their velocity. This allows to separate different electron energies by their location after passing through this field. The electron energy-loss spectrum (figure 9a) consists of a *zero-loss* peak (a large peak of all electrons that have not interacted with the sample at all) a low energy loss *plasmon* peak (plasmons are collective oscillations of the free electrons in the material), and a signal background (from multiple excitations and Bremsstrahlung) exponentially decreasing with increasing energy loss. On top of this background, ionisation edges with increased intensity are found at energies characteristic for the elements in the analyzed sample volume.
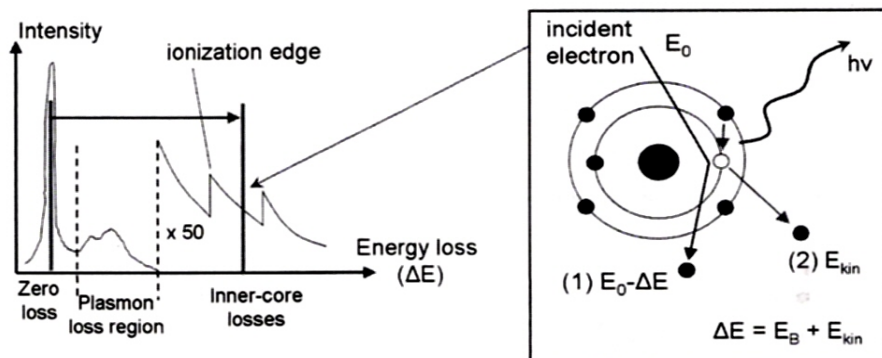
Figure 9. (a) an example of an EELS spectrum, (b) Schematic of the interaction of electrons with inner shell electrons [17].

24

EELS is a method well suited for light elements (except H and He) and for elements of medium atomic weight since scattering at light elements results in small energy losses. Therefore, it is complementary to EDS.

2.2.5.1. Energy-filtered transmission electron microscopy (EFTEM)

Since the binding energy E_b can be related to a specific element, EELS can be used to determine the composition on an area of interest by evaluating the ionization edges in the EELS spectrum. When an area of interest is imaged using only those electrons which show certain energy losses near an ionization edge, it is possible to acquire elemental maps similar to those obtained by EDX.

An energy selecting slit is applied below the viewing screen of the microscope (figure 8). An EFTEM image is always of a lower quality owing to the background signals in the EELS spectrum. However, the *three-window method* [17], [29] *can* reduce the influence of background signals. In this method, two pre-edge images and one post edge image are acquired on an area of interest. Subsequently, the background of the EELS spectrum is calculated based on the intensities of the electron energy losses within the two pre-edge windows (ΔE_1 & ΔE_2). The exponential background intensity function $I_b = C\Delta E^{-r}$ [29] is adjusted by variables C and r. By the use of this background function, the background integral $I_{3,b}$ is calculated, which may be subtracted from the total integral I_3 to obtain the background-reduced amount of all electrons showing losses within ΔE_3, i.e., I_s.
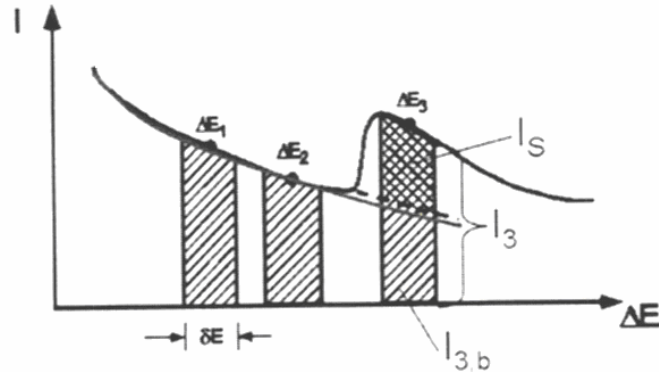
Figure 10. Schematic of the three-window method [17].

In the present thesis, EFTEM was used for chemical analysis in instances where the resolution of EDS was insufficient to separate certain elements on the basis of their X-ray energies (e.g. Mo and S).

2.3. An Introduction to Optical Beam Induced Current (OBIC) study of solar cells

The overall conversion efficiency of a photovoltaic device depends on the efficiency of every point of the photoactive surface. This depends on the underlying microstructure generated during the manufacturing process (semiconductor material growth, doping diffusion, texture structure, contaminants, etc.) [30]. A point-by-point characterization of the photovoltaic surface is therefore a powerful tool for an accurate and effective description of the device.

The OBIC (or sometimes called LBIC i.e. light/ laser beam induced current) method uses a highly focused light beam to irradiate the surface of the sample which is rastered relative to the illumination and the short circuit current flowing in the cell is measured while carriers are excited by the light beam, allowing maps or line-scans of performance to be collected. These maps reflect quantitatively the local variations in collection efficiencies. From the OBIC signal,

26

conclusions can be drawn on the local properties (local quality of junction, spatial variation in resistivity, local shunting effects, etc) of the investigated sample [31]. This technique therefore yields information directly applicable to the question of uniformity and the density of local defects. Local defects act as recombination centers for charge carriers reducing the optical beam induced current.

In previously reported OBIC work, a laser beam has been used as the source of illumination [31]. Besides laser, an electron beam can also be used to generate carriers and measure photocurrent. Such a setup is typically adopted inside a scanning electron microscope and is referred to as EBIC i.e. electron beam induced current [32]. Although the resolution of OBIC is less than that of EBIC (typically 2-4 µm), the OBIC/ LBIC technique is more relevant for these devices because carrier injection takes place in a manner analogous to normal operating conditions [33]. The spectral response can also be measured using other light sources like monochromated tungsten, halogen lamps, etc [33], although the spatial resolution is somewhat reduced for these sources.

An OBIC system can have the following combinations for rastering, (a) movable beam and a fixed stage, (b) a fixed beam and a movable stage or (c) mixed systems [30], [34]. The systems based on option (a) are generally faster than the others. They work by deflecting the laser beam according to a pattern similar to that followed by an electron beam in a TV set. These systems present some problems related to focusing when a large surface is scanned, since the distance between the deflecting device and the incident point is not constant. The systems based on option (b) do not pose deflection problems, although they are generally slower than the former, since the time they need to scan a surface is limited by the speed of the movement of the sample holder

system. This is not, however, the only necessary condition in order to obtain high spatial resolution photo-response maps. It is equally necessary that, in overall terms, the opto-mechanical device used for scanning the surface be free of fluctuations, in both its mechanical and optical aspects, being therefore capable of controlling with precision the exact position of the zone to be irradiated and the photonic stability of the beam used for irradiation. In case of light sources other than a laser, it is necessary to take into account the complex geometry of the emitting source. Problems like polychromatic nature of the emission can be dealt with by the use of a monochromator to select a narrow spectral range, at all times greater than the one which would correspond to a laser emission [30].

The light from the source is mechanically chopped (in cases where electrical modulation is not possible) and is synchronously detected by a lock-in amplifier. This is referred to as phase sensitive detection [31]. Electronically modulated light results in an AC signal on top of a DC light i.e. the illumination of other areas by light from the surrounding in general does not go to zero at any time which necessitates the use of a chopper. Disadvantages of using a chopper include poorer noise performance (due to vibration and jitter at the reference frequency) and that high-frequency components inherent in a square wave may result in complications to the solar cell response. The lock-in system multiplies the signal with a sine wave at the reference frequency thus decreasing the effective bandwidth.

The effect of background light (from the illumination and room background light) on the solar cell response can be complicated. Incident light can populate traps, and the resulting photocurrent can affect both the solar cell response and the electrical circuit response [31]. Background light at the reference frequency can introduce errors. The use of electronic intensity

28

modulation has the advantage of eliminating modulation of environment lighting sometimes associated with choppers. For these reasons, the entire apparatus needs to be covered thus allowing light only from the source to reach the sample.

CHAPTER 3. EXPERIMENTAL DETAILS

3.1. FIB milling with ex-situ lift-out

A *FEI 200 TEM Focused Ion Beam* system operating at 30 KV was used to prepare cross-sectional TEM samples of the solar cells. Milling was initiated with a current of 7000 pA to cut the trenches on either side of the Pt layer. As the milling progressed, the current was successively reduced with the thinning of the sample. Currents as low as 30 pA were used for the final thinning of the sample. The approximate dimensions of the final sample were 16μm (length) x 5μm (height) x 50 nm (thickness). The sample was lifted out using the ex-situ method. A *Mitutoyo VM Zoom 40* optical microscope equipped with hydraulic micromanipulators was used to lift out the sample from the bulk and place it on Cu grid in a manner described in section 2.1.1.

3.2. TEM study using BF imaging, EDS and EFTEM

A 300 kV *FEI TECNAI F30* Transmission Electron Microscope was used to study the microstructures of the thin-film solar cells. The Cu grid containing samples milled by the FIB was placed into a *FEI double tilt* holder. This allows tilting of the sample at various angles along two principal directions.

An optimum combination of electron beam intensity and CCD exposure time is required for BF imaging without saturating the CCD camera. The *Digital Micrograph* software was used to acquire and modify BF images.

In case of EDS, the sample was tilted typically by 12-15º. A STEM image was first acquired using the HAADF detector and then line scans (with 50-70 points on the line), point scans or drift corrected area scans (of typically 50*50 pixels) were obtained corresponding to this STEM image. Line scans were used to determine how the composition changes within a thin-film layer and across the various interfaces in thin-film solar cells. Elemental maps were used in certain critical areas to analyze rough interfaces and structural and chemical inhomogeneities in the absorber layer. Such an area acquisition takes a very long time in comparison to a point or a line scan and needs a drift correction to reduce the effects of specimen movement induced by, e.g., charging, to a minimum. STEM imaging and EDS results were analyzed using the *Tecnai Imaging and Analysis* software. EFTEM maps were obtained using the CCD camera. These maps were acquired typically with slit widths of 10eV (for low energy losses) or 30 eV (for high energy losses) using the three-window method to reduce the effects of background signals.

3.2.1. Difficulties in TEM characterization of thin-film solar cells

3.2.1.1. Overlap of X-ray energies for Mo-L and S-K

Certain elements have similar X-ray energies. This creates a problem in the identification and quantification of these elements in the sample. One such example is Mo and S. Mo-L and S-K have similar X-ray energies which cannot be distinguished by the EDX spectrometer. Thus, the identification of MoS_2 at the interface of $CIGS_2$ and Mo is a complicated issue since both Mo-L and S-K show up in the EDX spectrum as a cumulative signal at the Mo back contact corresponding to the X-ray energy of ~2.3 KeV.

Thus, MoS_2 can be detected only by separating the Mo signal from S. This can be done by calculating ratios of integrated intensities of (Mo-L + S-K) and Mo-K. A variation in this ratio at various points along the Mo layer is a strong indication of the presence of S (or S-K signal).

Other techniques like EELS/ EFTEM can be used in this case since the qualitative analysis is in terms of energy losses suffered by the electrons and not by the X-ray energies emitted.

3.2.1.2. Sample preparation issues with FIB

As mentioned in section 2.1, a FIB system uses Ga ions to image and mill the material to the required TEM thickness specifications. Introduction of Ga ions is a big disadvantage since the absorber layer also has Ga and this could lead to erroneous results. Ga introduction can be reduced my minimizing the use of 45º tilt to view the sample cross-section in the FIB system since this introduces the most amount of additional implanted Ga in the cross-section.

TEM samples can be prepared in the FIB at exact locations as desired by the operator. But the thickness of the TEM samples prepared in a FIB system is limited to 50-70 nm at best with about 10 to 20 nm amorphous layers on both surfaces caused by the radiation damage of the incident Ga beam. HRTEM requires FIB samples as thin as 10 nm. Thus a sample prepared by FIB cannot be used for high-resolution microscopy.

3.2.1.3. Cu signal from the TEM grid

The TEM grid consists of a thin amorphous film of carbon held within a Cu mesh (figure 3d). Thus a TEM sample would always show a Cu signal in the EDX spectrum from the grid. This creates a problem in quantifying the Cu already present in the absorber layer of the thin-film solar cell.

3.2.1.4. Quantification of EDS data

It is difficult to quantify EDX measurements especially in the case of thin-film solar cells. Quantification of EDS data needs the use of standards. It is impossible to produce CIGS/CIGS$_2$ layers that may be used as a standard for EDX measurements. This is because CIGS/CIGS$_2$ is a non-stoichiometric compound with an inhomogeneous distribution of elements. Also, each interface on its own consists of compounds with 5-6 different elements altogether making the quantification difficult due to the large number of elements involved. This limits the use of EDS as a qualitative tool which gives a variation in the concentration of elements with respect to each other.

3.3. Experimental setup for OBIC measurements

The equipment developed to measure optical beam induced currents consists of three sub-systems, namely, the *optics*, the *positioning system* and the *control and acquisition system.* The optics consists of a lamp, collimating lenses, apertures, beam steering mirrors, and an optical microscope. The positioning system has X-Y translation stages and a micropositioner for the front contact of the cell. The control and acquisition system consists of electronics to control the stages, a power supply to bias the cell, a lock-in amplifier-chopper assembly to measure the photocurrents and computer control to monitor the entire setup on a single screen. Figure 11 shows a schematic of the OBIC setup.

3.3.1. Optics

A *Spectra-Physics 69907* Xenon arc lamp emitting ultraviolet radiation provides the source of light for the setup. The lamp operates at 50 W by its power supply. The light from the lamp is

directed towards a series of collimating lenses through a 50 µm aperture, a mechanical chopper and a mirror into a *Nikon Optishot 66* microscope. The microscope has an internal semi-transparent mirror at 45º angle to tilt the incoming beam through an objective as a small probe onto the solar cell. The least possible spot size was 30-50 µm. The eyepiece on the microscope provides means to adjust the spot size on the cell surface. The entire optical assembly along with the lamp is mounted on a 23''X 47'' breadboard consisting of channels for the translation and positioning of the aperture, lenses, chopper and the mirror.

3.3.2. Positioning system

National Aperture MM-3M-EX motorized X-Y translation stages having a resolution of 0.5 µm were mounted on the microscope stage. The sample is mounted on a platform on these stages. A *Signatone* micropositioner with a fine tungsten needle, also mounted on this platform provides a mechanical contact to the front contact grid of the solar cell. A wire soldered to the back contact of the cell provided the other electrical contact. The assembly of the micropositioner and translation stages is enclosed inside a chamber coated with black cloth from inside to reduce the effects of outside light on the experiment.

3.3.3. Control and acquisition system

The controllers for the motorized translation stages are connected to the computer through an RS-232 interface. An *Agilent E3631A* DC power supply operating at +-6V provide the necessary bias to the solar cell in order to measure the voltage dependence of the collected photocurrent. A *Stanford Research Systems SR830* DSP lock-in amplifier is used to measure photocurrents and voltages at a frequency triggered by a *SR540* mechanical chopper. The chopper is mounted so as to modulate the illumination from the lamp at the desired frequency. A GPIB interface is

connected the computer to the lock-in amplifier. A circuit board consisting of switches and a 1 KΩ resistor provided means to switch between different choices of setups for voltage or current measurements with and without the power supply.
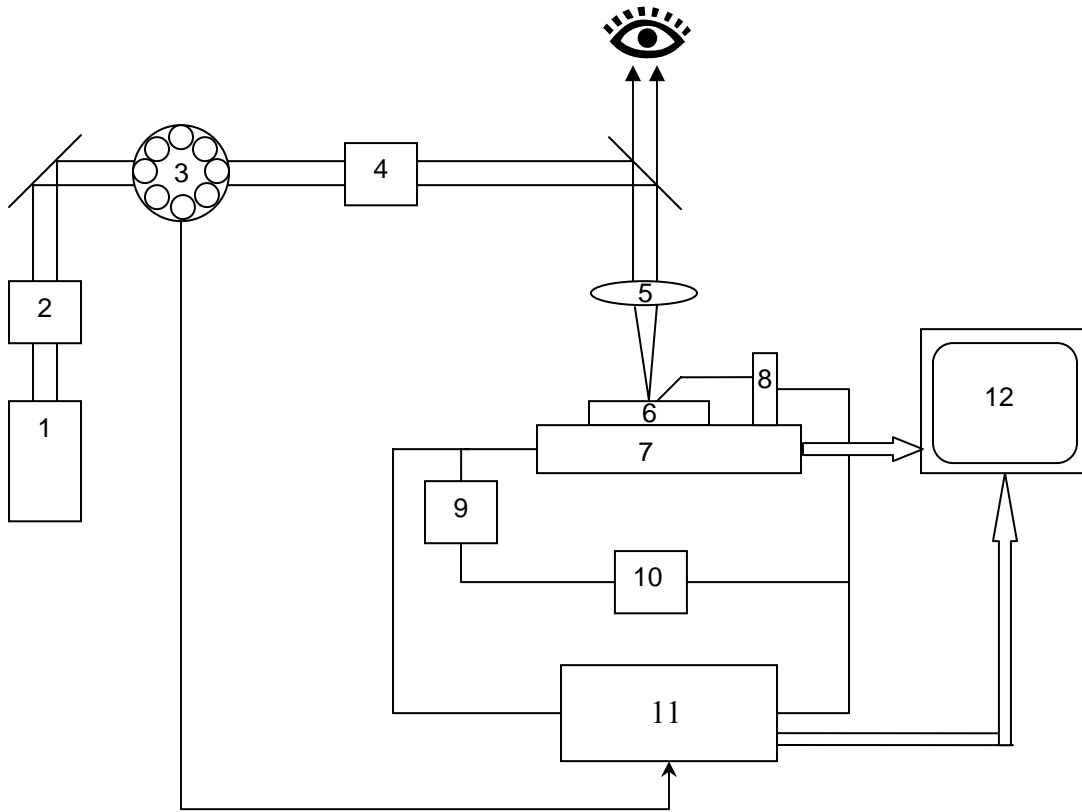
Figure 11. Schematic of the OBIC system

1. Xenon lamp, 2.Aperture& lenses, 3. Chopper, 4. Lenses, 5. Microscope objective, 6. Sample

7. X-Y translation stages, 8. Micropositioner with W needle, 9. Resistor, 10. DC power supply,

11. Lock-in amplifier, 12. Computer

In this thesis an extensive *LabVIEW* software control was developed to integrate the positioning system with the electronics. This allows for a control of experimental parameters on a single screen. A schematic of the program is as shown in the figure 12 a.

(a)

'For' loop (ii)

'For' loop (i)

1 2 3 4

READ (position, current/
voltage, phase shift)

S F S F S F

neg * no of loop (i) iterations

neg * no of loop (i) iterations

(b)

Sample

Scanning points

Figure 12. (a) A schematic of the LabVIEW program for the X-Y translation stages. Arrows indicate the direction of stage motion, S: start position and F: finish position for the stages. The numbers indicate the sequence of events.

(b) Schematic of scans to form an OBIC map. The circles indicate points of scan.

3.4. Operation of the OBIC setup

Before the actual operation of the equipment, a few procedures need to be followed. Care has to taken while mounting the sample. The sample should be flat with respect to the beam when the scan is in progress. This ensures that the beam is not out of focus at any point during the experiment. Also, the translation stages need to be aligned to scan the sample from the desired position.

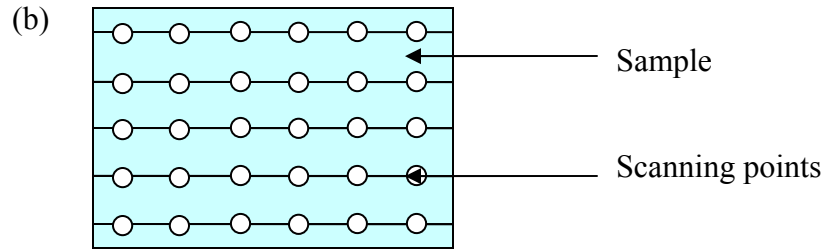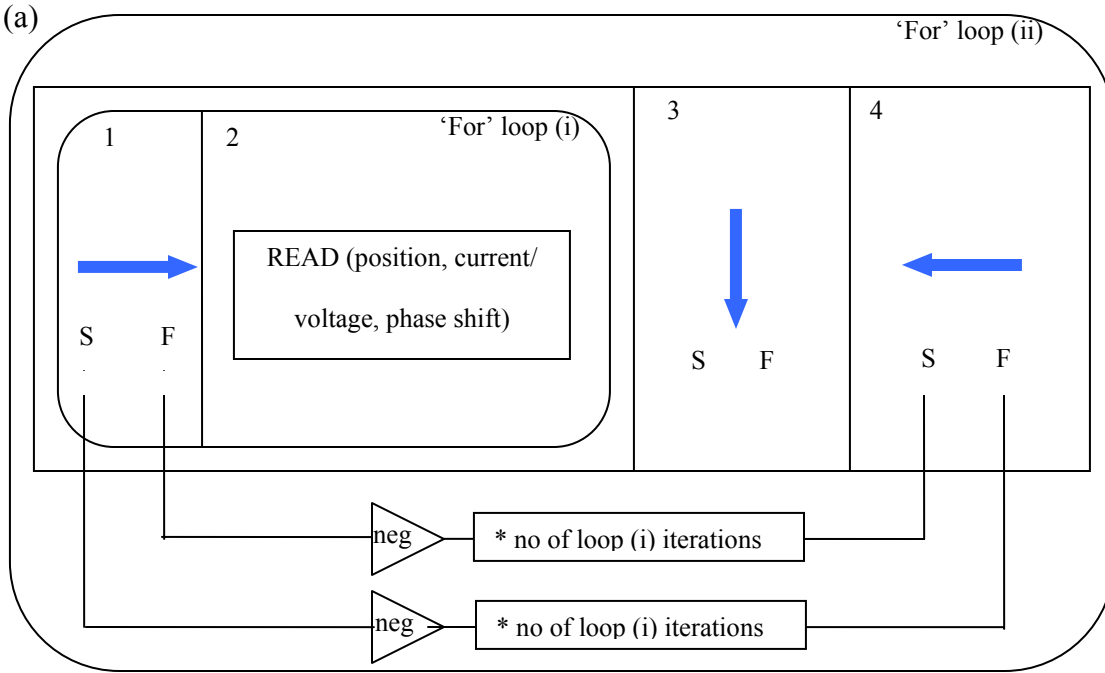The parameters of the scan are set by the operator using the LabVIEW interface. This includes the selection of starting and target positions and the 'for' loop iterations for the X-Y translation stages to set the pixel size of the OBIC map. The chopper frequency is kept constant throughout the course of the data acquisition. Maps are generated in a way shown by figure 12 b. Figure 13 shows the circuit diagram for the setup. By selecting the correct combination of switches S1, S2 and S3, following measurements are possible –

1. Voltage across the resistor (with and without bias)
2. Voltage across the solar cell (with and without bias)
3. Current in series with the solar cell and resistor (with and without bias)

The desired parameters (current/ voltage and phase shift) are measured on the lock-in amplifier. The SR830 is a dual-phase lock-in which gives parts of the signal in phase and 90º out of phase with the reference sine wave. Thus, the magnitude and the phase of the signal are available. To ensure best signal detection, the time constant (τ) and the sensitivity is optimized. The time constant is essentially the time over which the lock-in is looking over the signal. The sensitivity is easily set by using the auto-scale command.
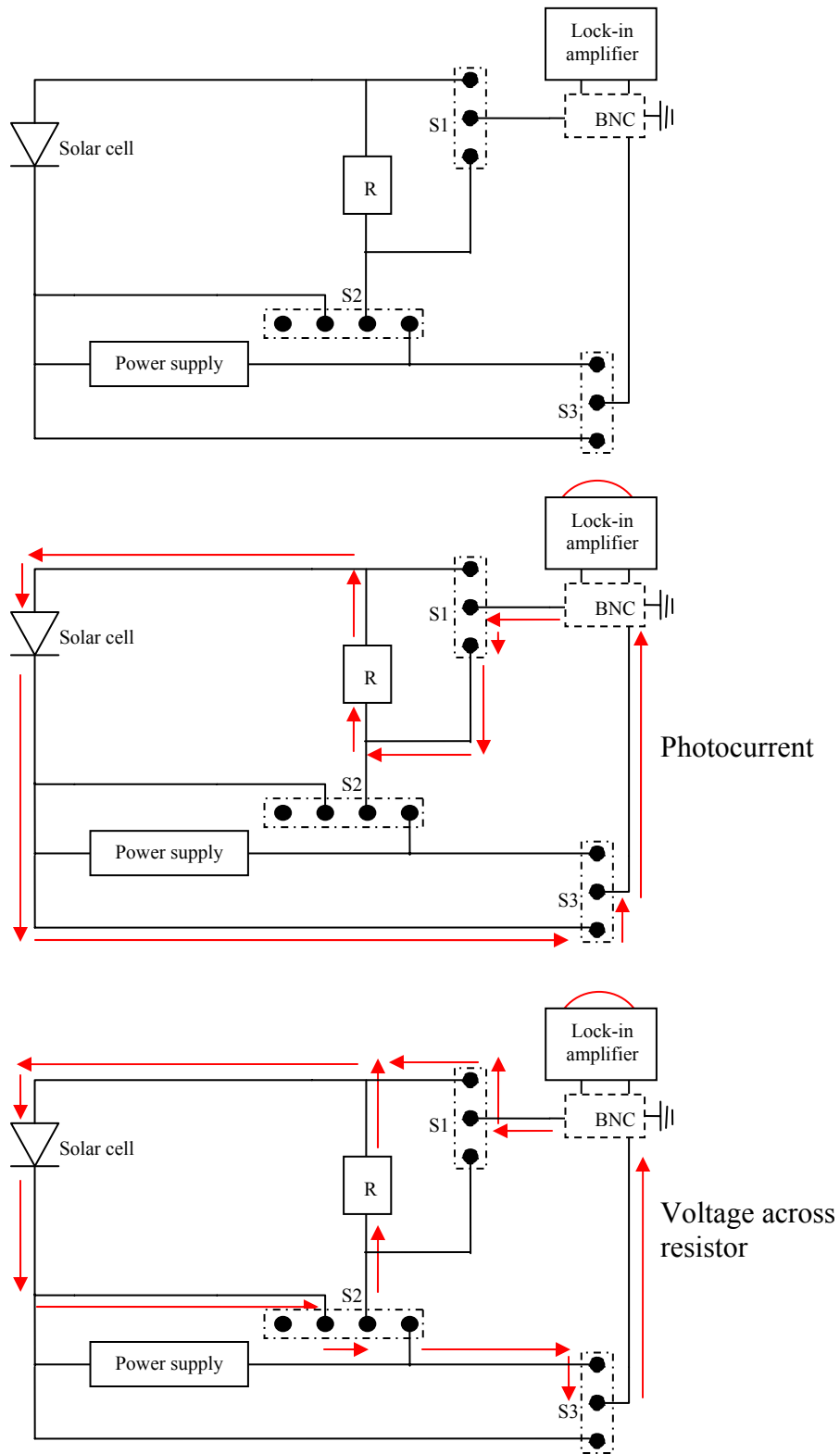
Figure 13. Circuit diagram to measure photocurrent and voltage. The switches connect neighboring lines depending on the setting.

CHAPTER 4. RESULTS AND DISCUSSION

4.1. Results from TEM analysis

4.1.1. Influence of the type of Na incorporation on the CIGS microstructure

The structural and chemical differences in CIGS-based thin-film solar cells with Na incorporation either by PDT or from SLG as previously described are reported in this section.

For PDT samples (figure 14b) with CIGS grown at lower temperatures (643 K), small columnar CIGS grains of about 100 nm diameter are observed close to the Mo back contact. The small lateral diameter of these grains is only slightly larger than the diameter of the Mo grains of the back contact. At higher temperatures (773 K and 853 K), the whole CIGS layer has large grains (about 1 µm) with only a few remaining small CIGS grains near the Mo back contact.

In samples without diffusion barrier (figure 14a) the small grain size near the Mo back contact is maintained up to 773 K while large grains (1 µm) are found near the CdS layer. For samples with a maximum deposition temperature of 773 K there is a distinct difference in the grain sizes near the Mo contact: A small grain size is found for samples without diffusion barrier, whereas a large grain size is evident throughout the whole CIGS layer for the PDT sample.

Samples treated at 643 K have a very rough CIGS surface at the CIGS-CdS interface. There is a decreasing surface roughness as the CIGS deposition temperature increases to 853 K. The CdS

(Na from SLG)

(a)

(Na from PDT)

(b)

ZnO

CIGS

Mo back contact   1 μm

←→ 643 K ←→

500 nm

Al grid
ZnO
CdS

CIGS

500 nm

Mo back contact

←→ 773 K ←→

500 nm

500 nm

←→ 853 K ←→

500 nm
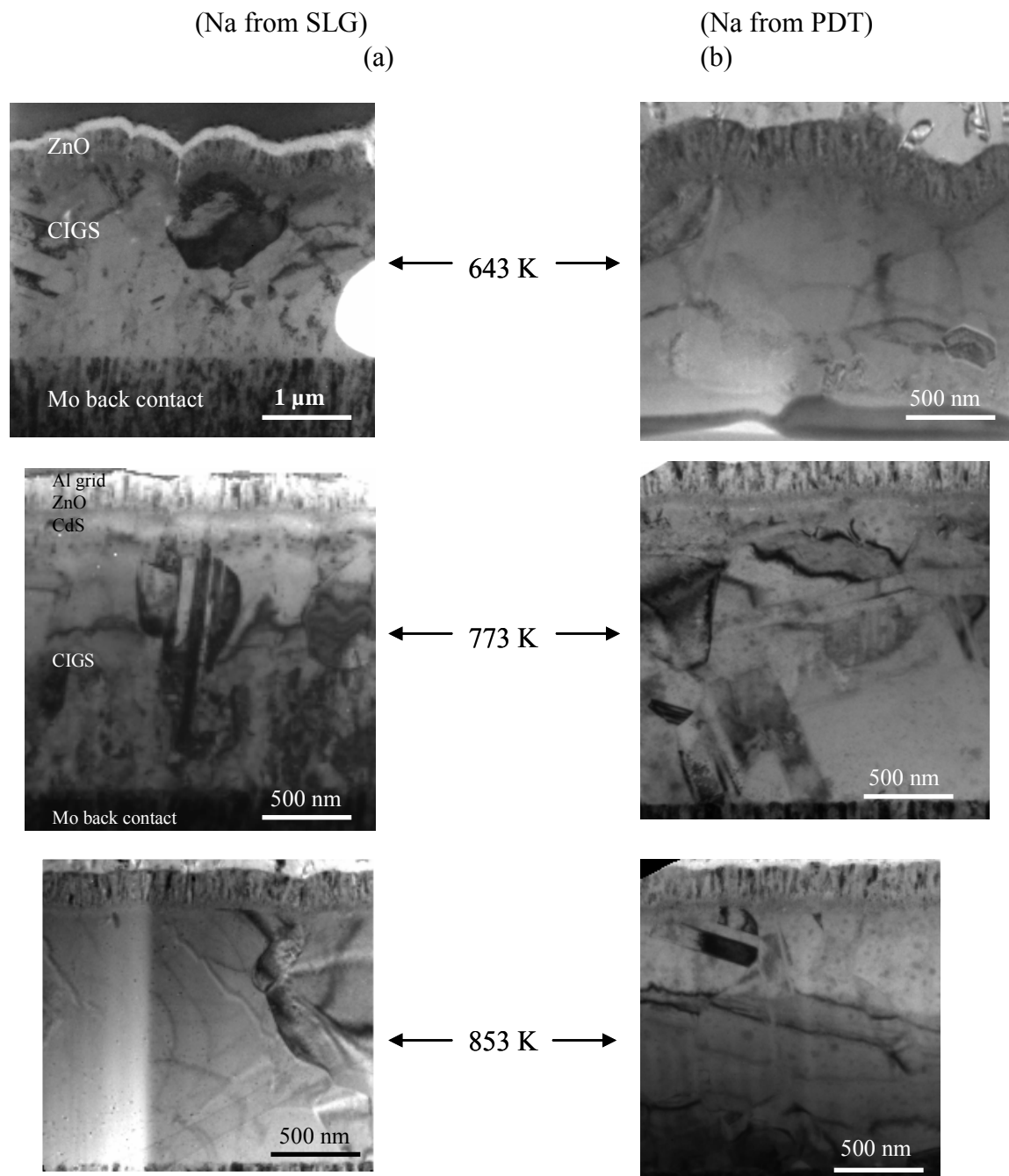
Figure 14. Cross-sectional bright-field images of CIGS-based thin-film solar cells with (a) and without (b) Al_2O_3 diffusion barrier

and ZnO layers are aligned with the CIGS surface, and even for high surface roughness the CdS coating is continuous, as shown in (figure 15).

A closer look at the rough CIGS-CdS-ZnO interface in the regions of high inward-curvature indicate the penetration of Cd and S into the CIGS layer possibly along trenches between grains near the interface as shown by the elemental distribution maps of Cd, S and Se (figure 15).
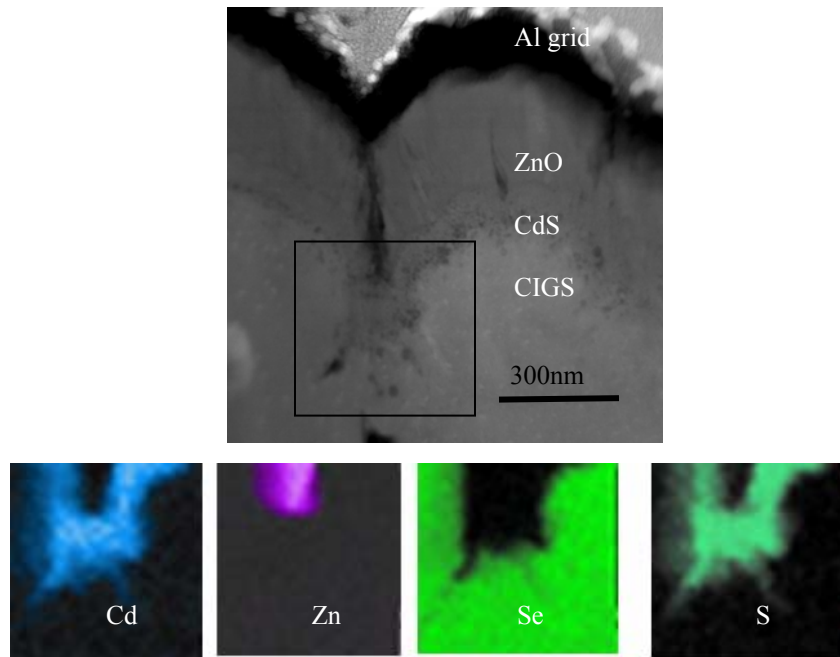
Figure 15. Cross-sectional HAADF-STEM image of the CIGS-CdS-ZnO interface and corresponding elemental maps. This PDT sample was prepared with a maximum deposition temperature of 643 K.

In the absorber layer small Cu-rich regions (<20 nm in diameter) were found in EDS distribution maps and line scans (figure 16). The EDS data show a locally enhanced Cu signal which is correlated with bright particles appearing in HAADF-STEM images. The X-ray signals from Se

and In are reduced in the regions of enhanced Cu content, while the Ga signal does not change. These particles are found both within CIGS grains and at grain boundaries in samples prepared at all deposition temperatures.
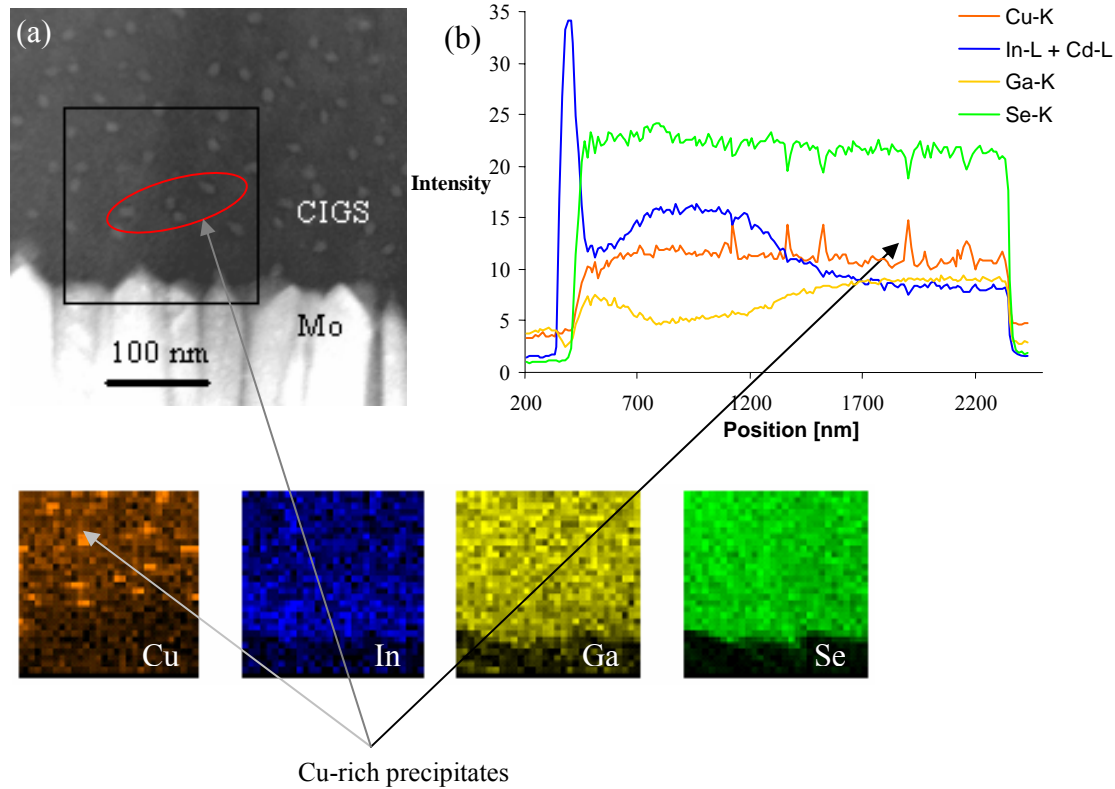
Figure 16. (a) HAADF-STEM image with EDS elemental distribution maps and (b) EDS line scan across CIGS layer (left: ZnO to right: Mo) for a PDT sample deposited at 673 K.

4.1.2. Effect of roughness of the absorber layer on top layers

Figure 17 shows the difference between a smooth and a rough CIGS surface. In the sample with smooth CIGS surface (figure 17a), the layers on top of CIGS are very even and continuous. In contrast, it has been difficult to maintain continuity of the CdS and ZnO layer in case of a rough

CIGS$_2$ absorber layer (figure 17b). In certain regions of high curvature of the CIGS$_2$ layer, complete coverage of ZnO on CIGS and CdS has been impeded leading to porosity (figure 17c).
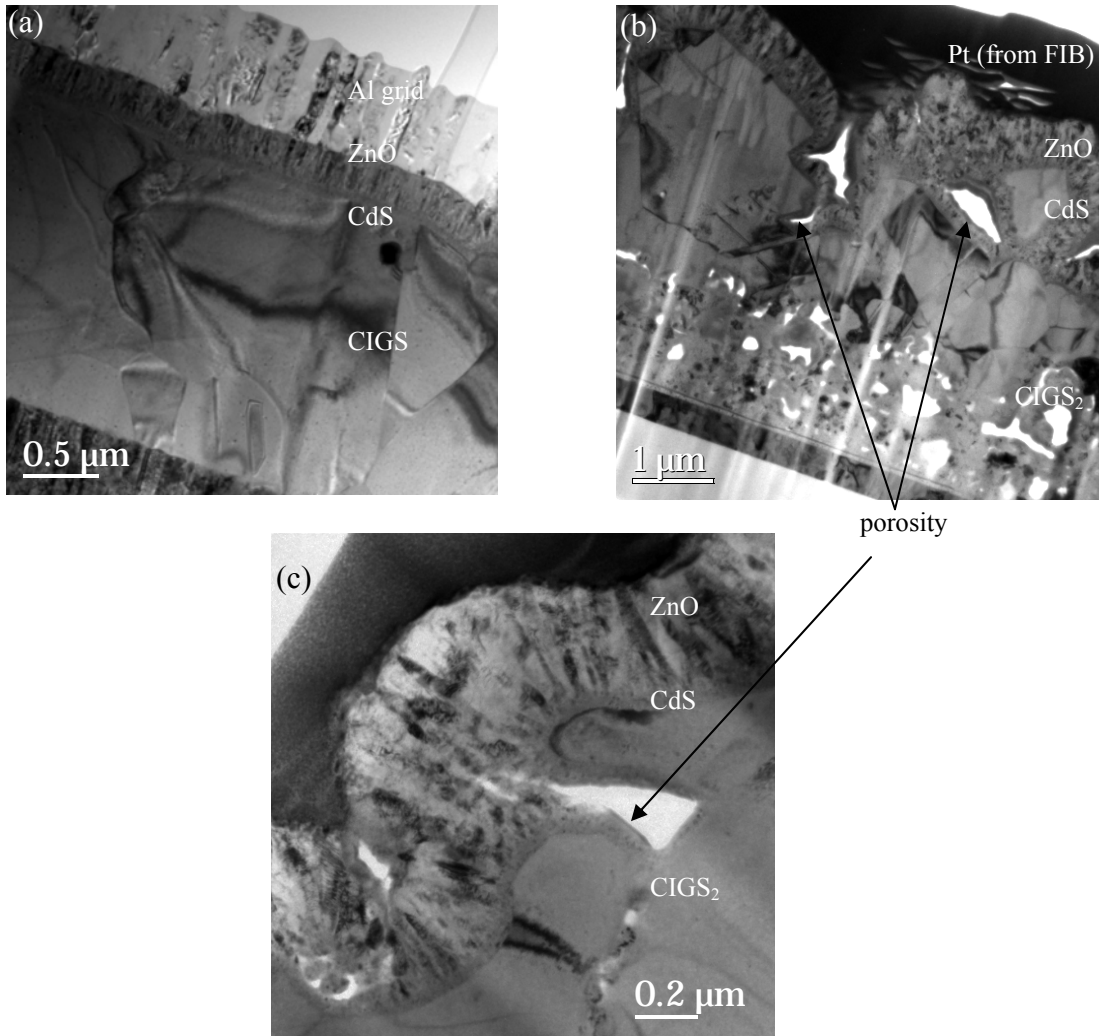
Figure 17. Cross-sectional bright-field images of (a) PDT sample with CIGS deposited at 853 K and (b), (c) CIGS$_2$ –based sample deposited on TCO-MoS$_2$ back contact.

For samples with Cr-Ag contacts with Cr close to the ZnO layer, there is a break in continuity of these contacts in regions of wavy CIGS$_2$ as indicated by the elemental maps in figure 18. The Cr and Ag layers have thicknesses of 50 nm and 500 nm respectively.
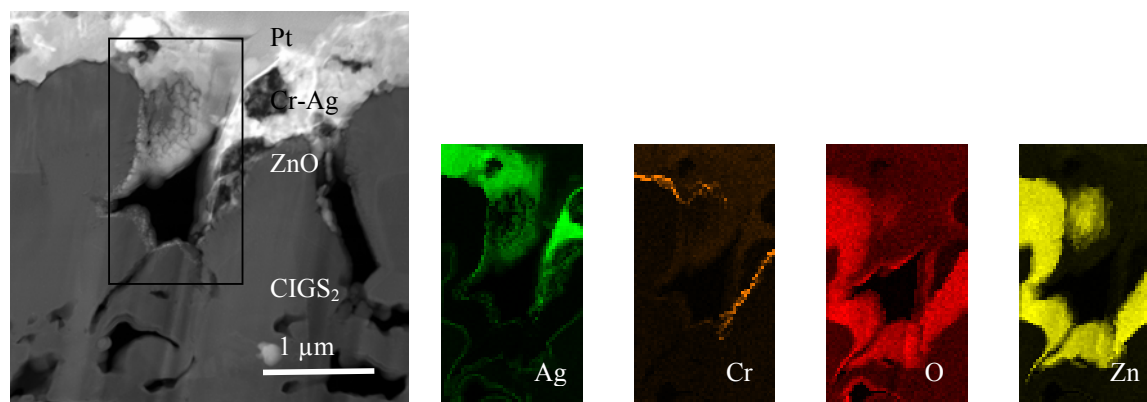
Figure 18. Cross-sectional HAADF-STEM image of the $CIGS_2$-CdS-ZnO interface and corresponding EDS elemental distribution maps.

4.1.3. Porosity of CIGS/CIGS$_2$ close to the Mo back contact

Some of the samples with CIGS/CIGS$_2$ absorber layers showed a varying degree of porosity close to the back contact. These samples were particularly the ones which did not have any Na incorporation by PDT or SLG. The porosity was restricted to only the bottom 1000 nm of CIGS/CIGS$_2$ where small grains of about 150 nm size are found. There was no penetration of porosity into the Mo or the MoS_2–ITO back contact as seen in figure 19.

Elemental line scans over the pores reveal the presence of Si and O along the edges of the pores. There is also a segregation of In close to the pores but on the outer edge of the Si and O signal (figure 20). Such an In segregation was not observed for all the pores.

The reason for porosity could be related to a TEM sample preparation effect in the FIB. Excessive thinning of the TEM sample cross-section can lead to porosity. Mo and MoS_2-ITO layers are not easily milled owing to their high hardness which could leave the porosity only in
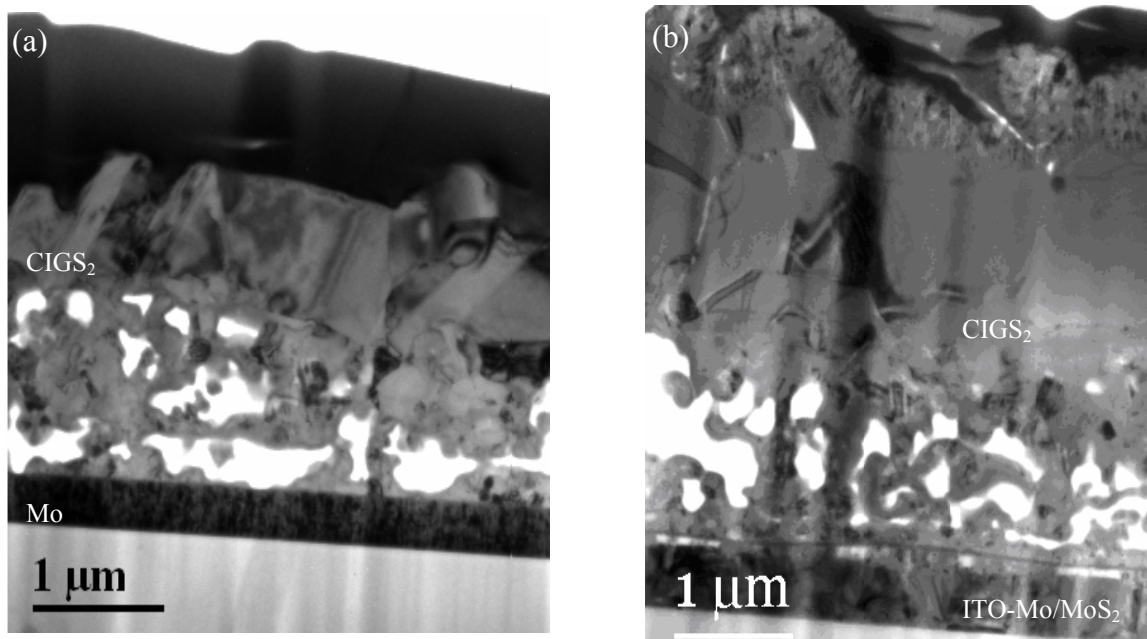
Figure 19. Cross-sectional bright-field images of thin-film solar cells with (a) CIGS$_2$ -Mo and (b) CIGS$_2$-ITO-MoS$_2$ interface.
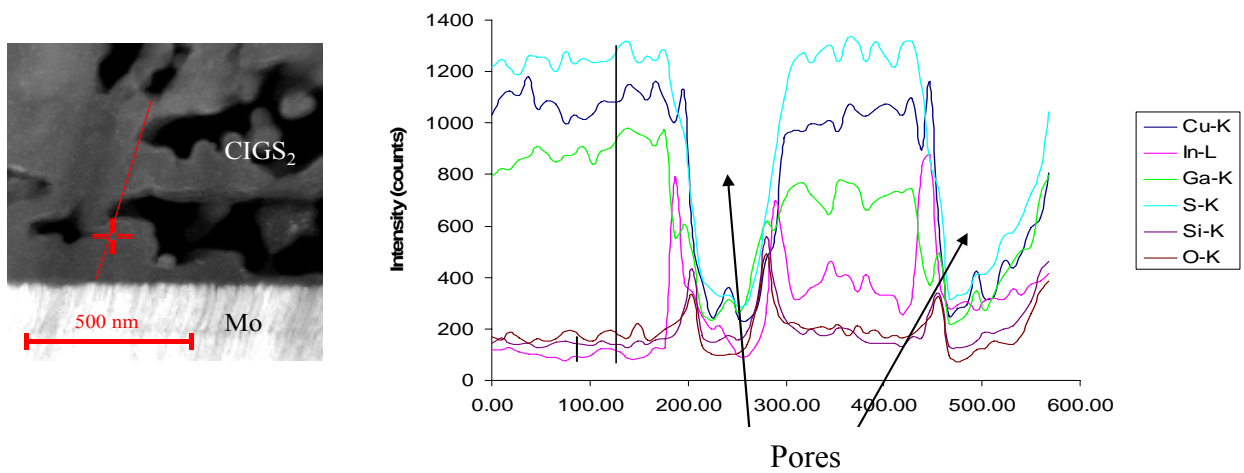
Figure 20. HAADF-STEM image (left) and elemental line scan (right) over the porosity in the CIGS$_2$ absorber layer.

the absorber layer. To verify that the porosity was not a result of excessive FIB thinning, the cross-section was studied in the FIB at 45º tilt (when it had a thickness of about 300-500 nm) before thinning it down to the required electron transparency of 50-70 nm. Figure 21 indicates the presence of pores in the bulk sample. Formation of pores could also be due to certain evaporation effects due to the use of a highly focused Ga beam in the FIB.
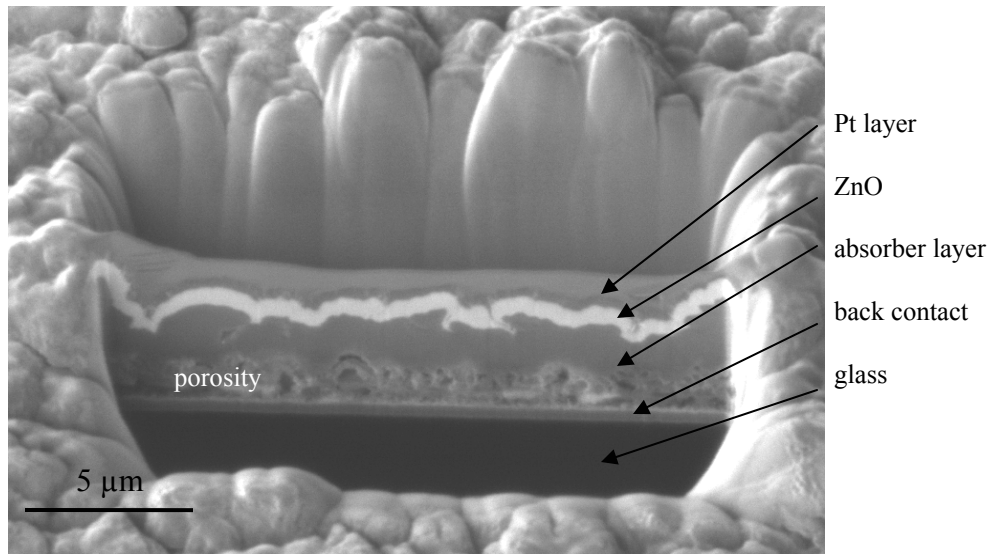
Figure 21. Cross-sectional FIB image of a thin-film solar cell indicating porosity close to the back contact.

4.1.4. Chemical heterogeneities in the absorber layer

4.1.4.1. Varying In/Ga ratios

The CIGS/ CIGS$_2$ /CIGSS absorber layers had varying In/Ga concentration ratios. While near the back contact of the absorber the Ga concentration was higher than In, the concentration ratios were reversed close to the CdS layer with the crossover of the ratios around the central region of the absorber as shown in the line scans and elemental maps in figure 22.
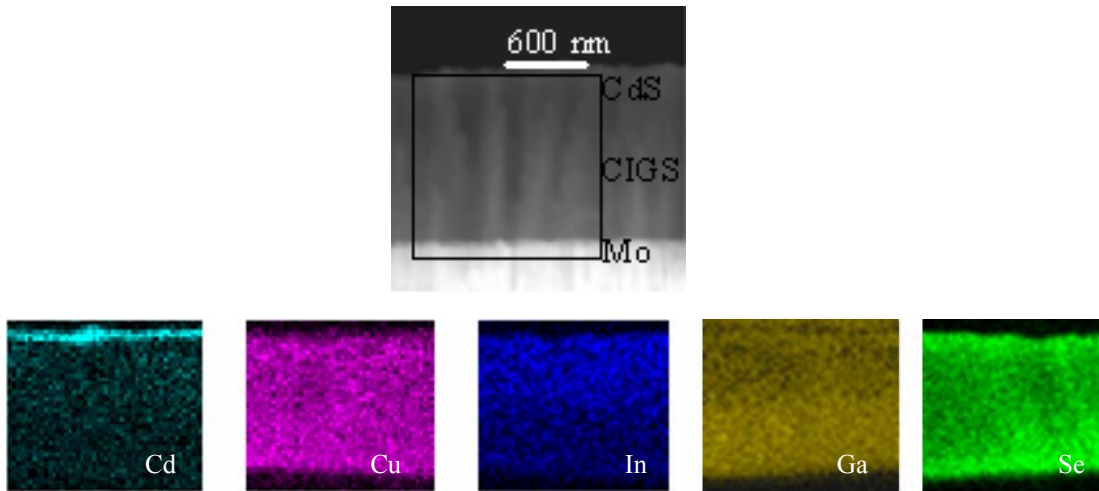
Figure 22. HAADF-STEM image and elemental distribution maps showing In-rich and Ga-deficient part of the CIGS layer.

4.1.4.2. Heterogeneous segregation close to the back contact

Other chemical heterogeneities observed were the formation of deposits. Some of the $CIGS_2$ samples showed increased amounts of Se close to the back contact. This selenium was not intentionally added to the $CIGS_2$ layer. If the same chamber is used for sulfurization (to form $CIGS_2$) and for selenization (to form CIGS), there could be contamination in the absorber layer from either of these elements. Selenium seems to be present at the expense of In (figure 23a). Some other samples showed Cu-Ga rich regions (figure 23b). Probably these regions remained unsulfurized leading to these deposits.
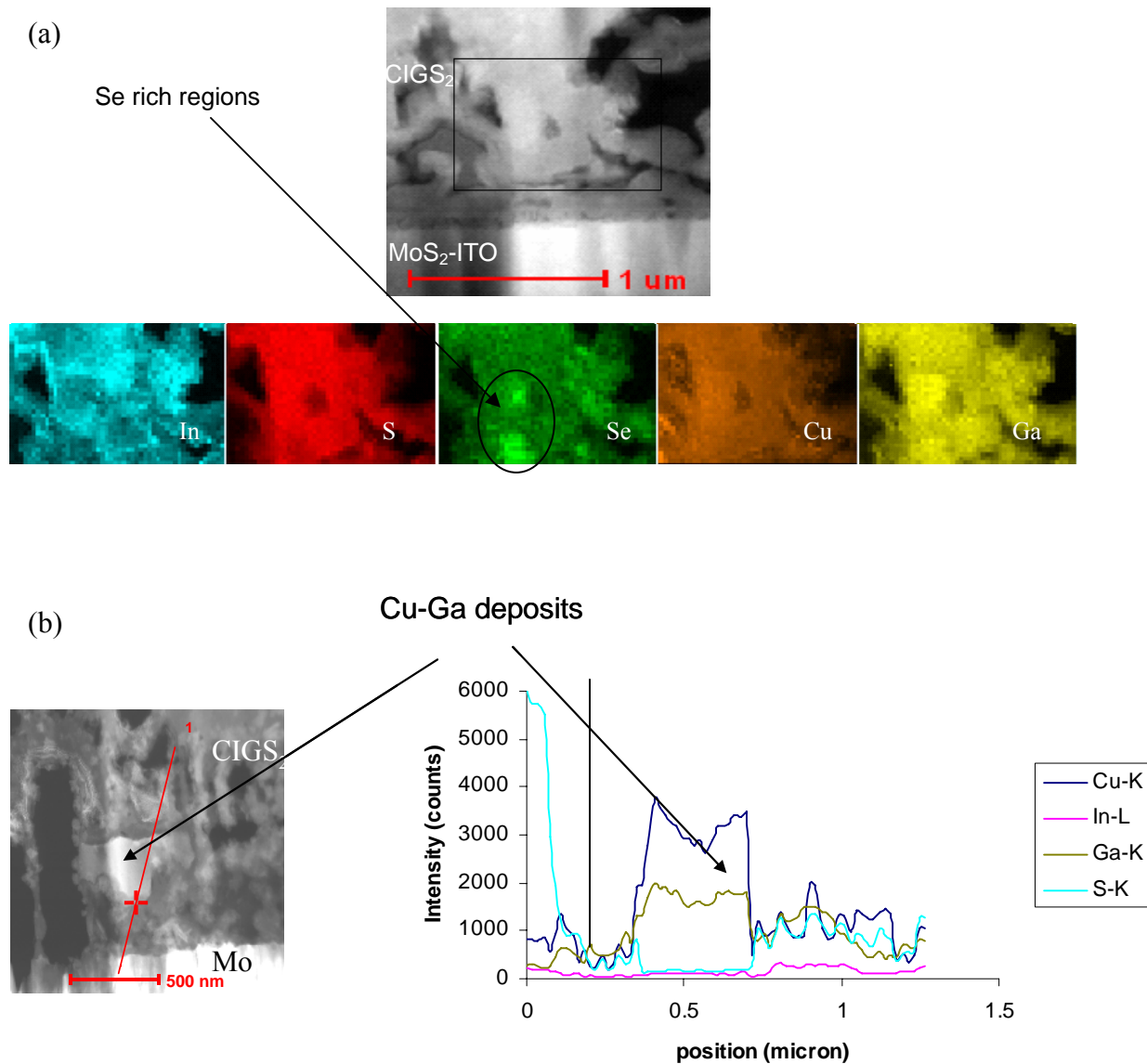
Figure 23. HAADF-STEM image and (a) Elemental maps and (b) line scan across $CIGS_2$ layer indicating presence of Se and Cu-Ga rich regions respectively.

4.1.5. Diffusion of $CIGS_2$ through Mo in $CIGS_2$ –Mo/MoS_2- ITO type configuration

To form a transparent back contact, an ITO layer was deposited on glass followed by a 10 nm layer of Mo. A $CIGS_2$ layer was then deposited over it. During sulfurization, Mo converts to MoS_2 thus forming an ITO-Mo/MoS_2 back contact. Observation of the $CIGS_2$ –Mo/MoS_2-ITO

48

interface reveals the presence of a 200-300 nm thick Cu-In-S rich layer between the 10 nm MoS_2 layer and the ITO (figure 24) It appears that Cu and S diffuses through the thin MoS_2 layer and reacts with In from the ITO to form a $CIGS_2$ layer with reversed In/Ga ratio compared to the ratio above the Mo layer (figure 24b).
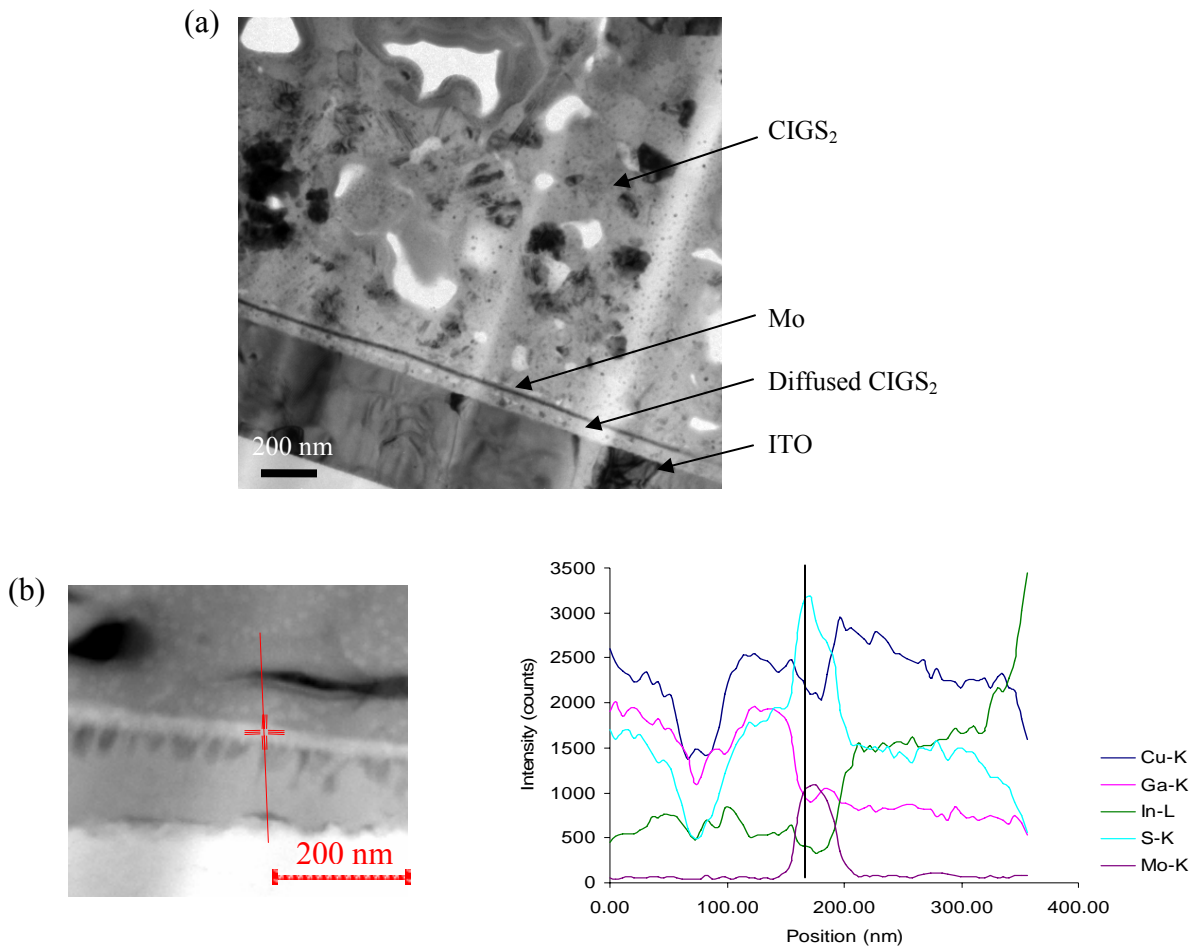
Figure 24. (a) Cross-sectional bright field image and (b) HAADF-STEM image with elemental line scan over the $CIGS_2$ –Mo/MoS_2- ITO interface.

EDS results are inconclusive in determining the presence of a MoS_2 layer since the X-ray energies of Mo-L and S-K are very similar. EFTEM was used to determine whether the 10 nm Mo layer deposited on ITO was converted to MoS_2 during sulfurization.
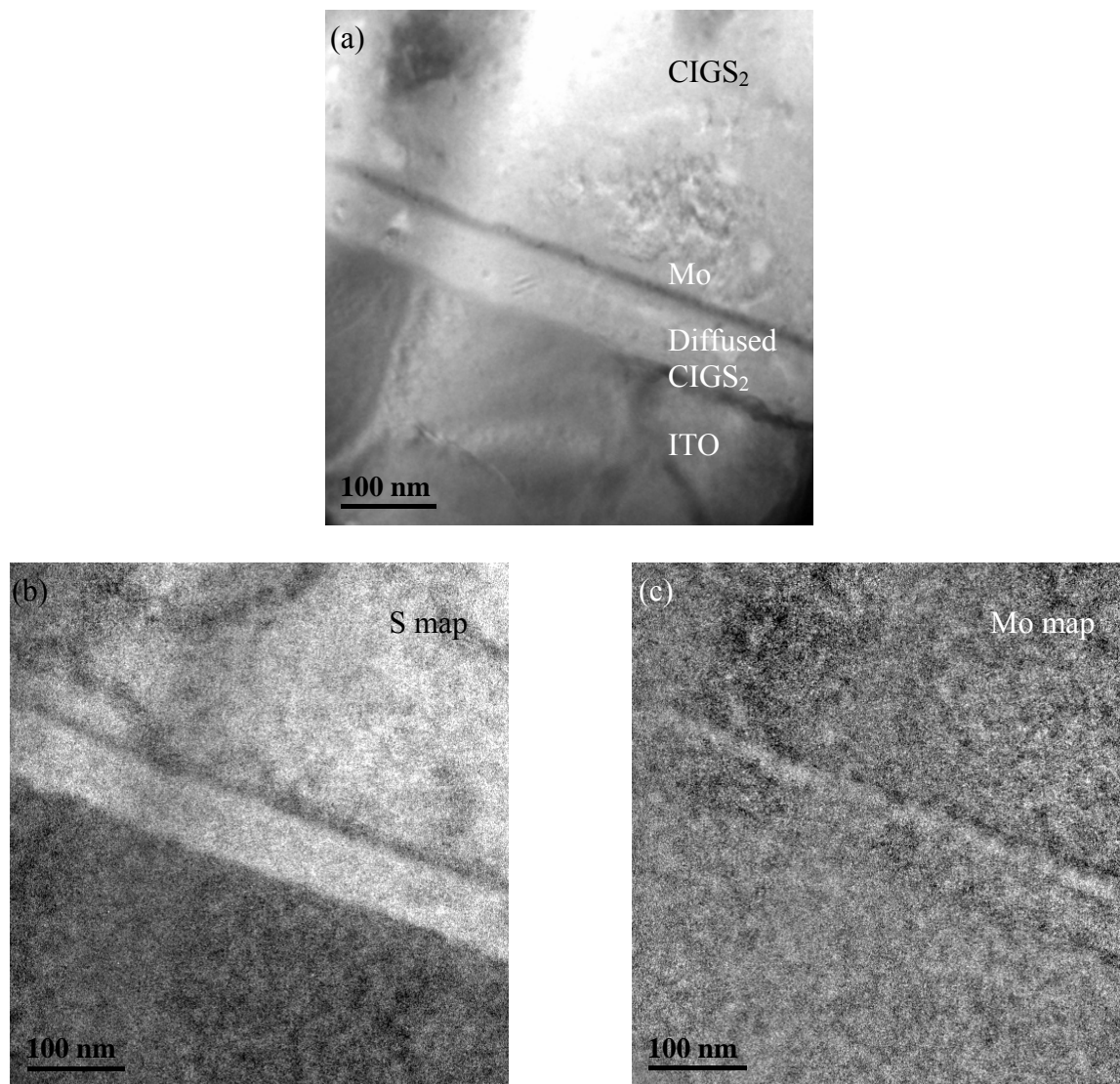
Figure 25. (a) Bright-field image and (b) & (c) EFTEM maps at the $CIGS_2$ –MoS_2 –ITO interface

The EFTEM maps (figures 25b & 25c) indicate the absence of S within the Mo layer giving hints that the Mo layer may not have been converted into MoS_2 during sulfurization.

4.1.6. Formation of MoSe$_2$ at the CIGS/ CIGSS- Mo interface

Some of the CIGS/ CIGSS samples revealed the presence of a continuous Mo-Se rich (probably MoSe$_2$) layer at the interface of CIGS/ CIGSS with Mo (figures 26 & 27). This was confirmed by a line scan across the Mo/ MoSe$_2$/ CIGSS (or CIGS) interface: the Se signal is twice as large as the Mo signal (figure 27b). This layer was approximately 50-70 nm thick and showed good adhesion with the Mo back contact. Such a Mo-Se layer can be considered as buffer layer between the absorber and Mo which aids the formation of a low-resistance electrical back contact [35].
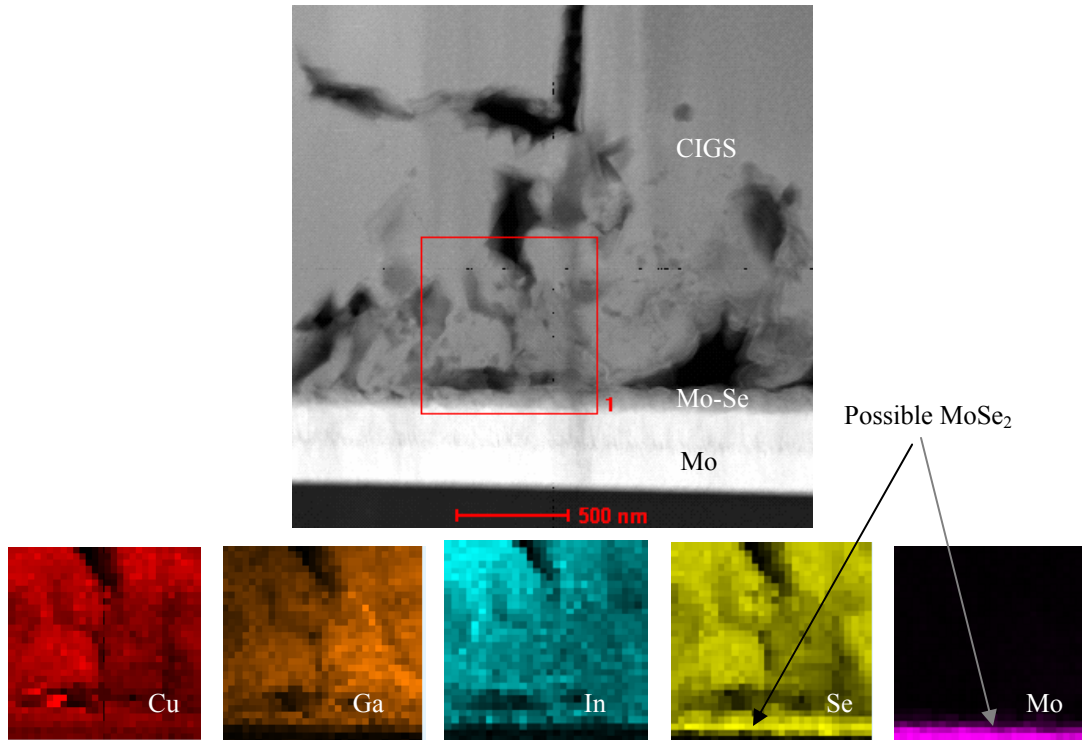
Figure 26. HAADF-STEM image and elemental map at the CIGS-MoSe$_2$ - Mo interface
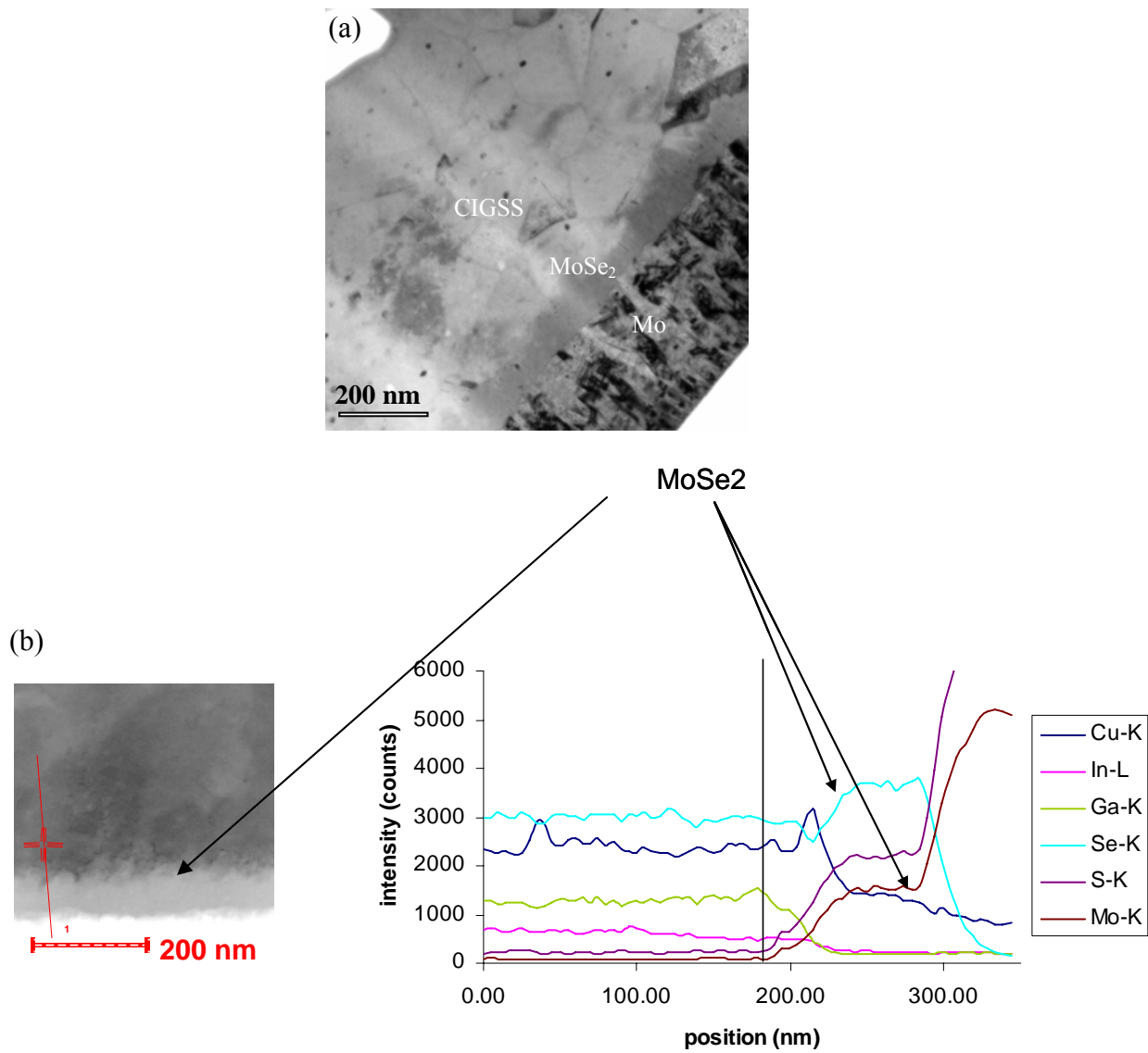
Figure 27. (a) Cross-sectional bright-field image and (b) HAADF-STEM image with elemental line scan across CIGSS-MoSe$_2$ –Mo

4.2. Results from OBIC measurements

Preliminary OBIC maps were generated using data collected by the lock-in amplifier. *MATLAB* software was used to plot a 3-D surface of the X-Y stage positions and the corresponding photocurrents (typically in nA) measured. The phase shift between the illumination and the chopped signal was also recorded for each reading and was observed to be constant for a given chopper frequency throughout the course of the experiment. Besides photocurrent, maps of the voltage drop across the resistor/ solar cell were also generated at zero bias. These results were similar to the photocurrent measurements with the voltage (typically in mV) dropping in defect areas.

Figure 28 shows an example of such 3-D surface. The data from the XY translation stages is in the form of 'motor rotations'. 1 'motor rotation' corresponds to 0.5 µm. Such a surface gives an idea about areas where collection of photocurrent is low. This corresponds to defects, surface blemishes and the front contact fingers which block the illumination of the absorber layer. A 20-25 % variation in photocurrent is observed between defect and defect-free areas (excluding the front contact grid where the photocurrent drops to zero). Besides the X-Y stages, the resolution of such a map is highly dependent on the spot size of the probe. Spot sizes as low as 30-50 µm were used.
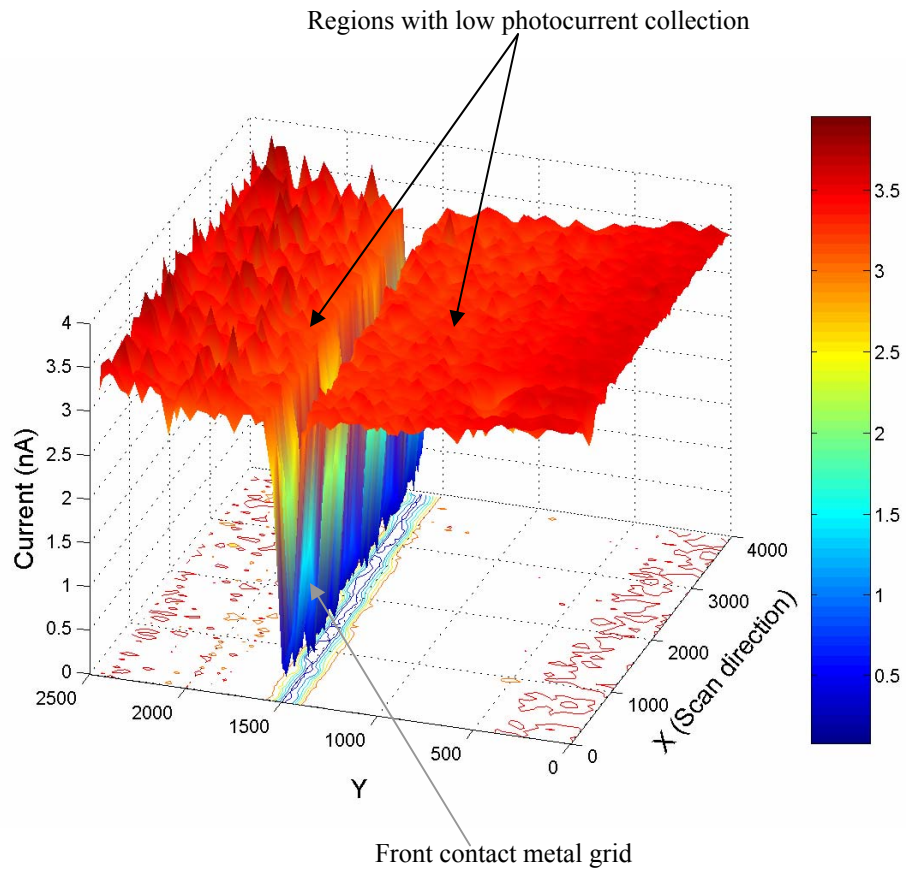
Figure 28. A 3-D plot showing variation in photocurrent with XY stage motion at zero bias. This is a 80 (X) * 50 (Y) pixel scan with a step size of 50 motor rotations (25 µm) in both X and Y directions. The area scanned is about 2 mm* 1.2 mm.

CHAPTER 5. CONCLUSIONS

5.1. Dependence of the CIGS layer morphology on the Na incorporation strategy

The comparison of different Na incorporation methods from SLG and PDT reveals the disappearance of small columnar CIGS grains close to the Mo back contact as a function of deposition temperature. For samples with a maximum deposition temperature of 773 K, the CIGS grain structure depends on the kind of Na incorporation strategy: PDT yields a uniform CIGS grain structure across the whole layer, while small CIGS grains are observed for samples without the diffusion barrier. For higher maximum deposition temperatures a similar tendency of slightly larger grains in PDT samples is observed.

The smoothness of the CIGS-CdS interface increases with increasing temperature and yields a flat CIGS surface at higher temperatures. The method of Na incorporation (Na from PDT or from SLG) however has no influence on the surface roughness.

5.2. Influence of a rough absorber layer on the top layers

Porosity between the absorber and the subsequent layers on top is observed in the samples from FSEC. ZnO and Cr-Ag contacts do not seem to provide a conformal coverage to the CIGS and CdS layers. A wavy ZnO layer also leads to an uneven distribution of the inherent i-ZnO and ZnO:Al layers. Discontinuities in the ZnO and Cr-Ag layers may affect the electrical conductivity in these regions and thus the overall electronic properties of the cell.

The CdS layer in all the samples is continuous with a good adherence to the absorber layer. This is observed even in case of a rough absorber layer. This highlights the advantageous CBD process used for this deposition step.

5.3. Porosity in the absorber layer

The reason for the formation of pores in the absorber layer remains unclear. One of the reasons could be certain evaporation effects in the highly focused Ga beam of the FIB. Porosity could also be a product of the deposition process since only the samples from FSEC have pores in the absorber layer close to the back contact. The presence of pores indicates either a multiphase material occurring during the deposition of the absorber layer, with one phase being volatile and evaporating in the Ga ion beam, or the actual formation of pores during deposition of this layer. In both cases, modifications of the deposition process appear necessary. Incidentally, the back contact remains intact with no traces of porosity. If porosity is a sample preparation effect, methods other than the FIB technique need to be employed. One of the successful bulk sample preparation methods previously used for obtaining TEM samples of thin-film solar cells include cutting the cross-section into thin stripes, embedding them with epoxy into a tube which is subsequently cut into disks that are dimple grinded and finally ion-milled to obtain cross-sectional samples [36].

The segregation of Si and O around the pores could possibly occur if a FIB cut is made deep into the glass substrate causing back deposition of Si and O along the pore surfaces.

5.4. Use of ITO- Mo/ MoS$_2$ back contact for CIGS$_2$ absorbers

The possibility for the use of TCO (ITO) as a back contact material has been explored to allow those photons having energies less than the band-gap energy of the absorber layer (and thus unabsorbed by CIGS$_2$) to be passed through it. A thin Mo layer (10 nm) deposited on to the ITO does not prevent the diffusion of CIGS$_2$ through it onto the ITO. Thus, the ITO-Mo/MoS$_2$ back contact is not intact and will not provide an ohmic contact to the ITO layer. The composition of the diffused CIGS$_2$ is however not the same as the one above the Mo layer. This may cause a variation in its band-gap and thus the purpose of using ITO would be lost. The EFTEM maps give strong hints that MoS$_2$ does not form at this specific Mo-CIGS$_2$ interface and hence the contact between CIGS$_2$ and Mo may not be ohmic. All of the above results are reflected in the low efficiency values reported for these types of cells.

5.5. Formation of MoSe$_2$

Though the formation of the stoichiometric MoSe$_2$ phase is not confirmed, it can be concluded that a Mo-Se rich layer is formed at the CIGS/CIGSS-Mo interface with higher Se concentration than Mo. Diffraction studies on the Mo-Se layer are inconclusive since the sample and the amorphous layers were too thick. Such a Mo-Se rich layer would provide an ohmic contact between the CIGS/CIGSS-Mo interface.

5.6. Other chemical heterogeneities

There is an increase in the Ga/In ratio from the top to the bottom of the cell. Such a band-gap grading improves the absorption of photons in the absorber layer. The presence of Se in CIGS$_2$ cells from FSEC could be due to the use of the same chamber for selenization and sulfurization

for the development of CIGS and CIGS$_2$ respectively. The unsulfurized metallic Cu-Ga deposits are defects in the CIGS$_2$ layer which can act as recombination centers for electrons and holes. The reason for the formation of Cu deposits 20 nm in size in the absorber layer is not clear. This seems to be a sample preparation effect since all the samples under the present study indicate the presence of these Cu deposits. These deposits may be formed due to certain decomposition effects in the Ga beam of the FIB and could possibly be metastable phases developing with time.

5.7. Remarks on OBIC measurements

An OBIC system was installed and its working principle was proven. Photocurrents were measured without the application of a voltage bias and high resolution maps were generated for the identification of defect-prone regions of a thin-film solar cell with undesirable optical properties. This system will be used in the selection of regions from where a FIB sample can be obtained for TEM analysis. The study of these special regions of a device will help in the identification of defects responsible for reduced conversion efficiencies and large-scale homogeneity of properties.

PUBLICATIONS AND PRESENTATIONS

- *'Defects and interfaces in Cu(In,Ga)Se$_2$-based thin-film solar cells with and without Na diffusion barrier'*, H. Heinrich, S. Senapati, S.R. Kulkarni, A.R. Halbe, D. Rudmann, A.N. Tiwari, Mater. Res. Soc. Symp. Proc. **865** (2005) 137-142.

- *'Defects and interfaces in Cu(In,Ga)Se$_2$-based thin-film solar cells with and without Na diffusion barrier'* H. Heinrich, S. Senapati, S.R. Kulkarni, A.R. Halbe, D. Rudmann, A.N. Tiwari. Poster presented at the MRS spring 2005 conference in San Francisco, CA.

- *'Defect characterization of Cu(In,Ga)Se$_2$ and Cu(In,Ga)S$_2$ absorber layers in thin-film solar cells'*, Ankush Halbe, Helge Heinrich, Sean Niemi, Anant Jahagirdar, Ankur Kadam. Poster presented at the FLAVS-FSM 2006 symposium in Orlando, FL.

- *'The interface between absorber layer and back contact in Cu-In-Ga-Se-S based thin-film solar cells'*, Ankush Halbe, Helge Heinrich, Neelkanth Dhere, Anant Jahagirdar, Ankur Kadam. Poster presented at the 2006 Graduate Research Forum at UCF, Orlando, FL.

LIST OF REFERENCES

1. M.D.Archer, "The past and present in: Clean electricity from photovoltaics", Imperial College Press, London (2001).

2. D.M.Chapin, C.S.Fuller & G.L.Pearson, "A new silicon p-n junction photocell for converting solar radiation into electrical power." *Journal of Applied Physics* **25**, 676 (1954).

3. K.L.Chopra, P.D.Paulson & V.Dutta, "Thin-film solar cells: An overview". *Progress in Photovoltaics* **12**, 69-92 (2004).

4. M.A.Green, K.Emery, D.L.King, S.Igari & W.Warta, "Solar cell efficiency tables (version 25)". *Progress in Photovoltaics* **13**, 49-54 (2005).

5. X.Wu, J.C.Keane, R.G.Dhere, C.DeHart, D.S.Albin, A.Duda, T.A.Gessert, S.Asher, D.H.Levi & P.Sheldon, "16.5% efficient CdS/CdTe polycrystalline thin-film solar cells". *Proceedings of the 17th European Photovoltaic Solar Energy Conference,* **2**, 995-1000 (2002).\

6. A.Jahagirdar, "Solar driven photoelectrochemical water splitting for hydrogen generation using multiple bandgap tandem of CIGS2 PV Cells and thin film photocatalyst". PhD thesis, University of Central Florida (2005).

7. F.Kessler & D.Rudmann, "Technological aspects of flexible CIGS solar cells and modules". *Solar Energy* **77**, 685-695 (2004).

8. N.G.Dhere, S.R.Ghongadi, A.H.Jahagirdar, M.B.Pandit & D.Scheiman, "CIGS2 thin-film solar cells on flexible foils for space power". *Progress in Photovoltaics* **10**, 407-416 (2002).

9. D.Rudmann, A.F.daCunha, M.Kaelin, F.Kurdesau, H.Zogg, A.N.Tiwari & G.Bilger, "Efficiency enhancement of Cu(In,Ga)Se-2 solar cells due to post-deposition Na incorporation". *Applied Physics Letters* **84**, 1129-1131 (2004).

10. D.Rudmann, "Effect of sodium on growith and properties of CIGS thin film solar cells". PhD thesis, Swiss Federal Institute of Technology Zurich, Diss ETH Nr. 15576 (2004).

11. M.Terheggen, "Microstructural changes in CdS/CdTe thin-film solar cells during annealing with chlorine". PhD thesis, Swiss Federal Institute of Technology Zurich, Diss ETH Nr. 15214 (2003).

12. P.J.Rostan, J.Mattheis, G.Bilger, U.Rau & J.H.Werner, "Formation of transparent and ohmic ZnO:Al/MoSe2 contacts for bifacial Cu(In,Ga)Se2 solar cells and tandem structures". *Thin Solid Films* **480-481**, 67-70 (2005).

13. N.Romeo, A.Bosio, V.Canevari, M.Terheggen & L.V.Roca, "Comparison of different conducting oxides as substrates for CdS/CdTe thin film solar cells". *Thin Solid Films* **431**, 364-368 (2003).

14. A.Romeo, M.Terheggen, D.Abou-Ras, D.L.Batzner, F.J.Haug, M.Kalin, D.Rudmann, & A.N.Tiwari, "Development of thin-film Cu(In,Ga)Se-2 and CdTe solar cells". *Progress in Photovoltaics* **12**, 93-111 (2004).

15. K.Ramanathan, M.A.Contreras, C.L.Perkins, S.Asher, F.S.Hasoon, J.Keane, D.Young, M.Romero, W.Metzger, R.Noufi, J.Ward & A.Duda, "Properties of 19.2% efficiency ZnO/CdS/CuInGaSe2 thin-film solar cells". *Progress in Photovoltaics* **11**, 225-230 (2003).

16. A.M.Gabor, J.R.Tuttle, M.H.Bode, A.Franz, A.L.Tennant, M.A.Contreras, R.Noufi, D.G.Jensen & A.M.Hermann, "Band-gap engineering in Cu(In,Ga)Se-2 thin films grown from (In,Ga)2Se3 precursors". *Solar Energy Materials and Solar Cells* **41-2**, 247-260 (1996).

17. D.Abou-Ras, "Structural and chemical analysis of buffer layers in Cu(In,Ga)Se2 thin-film solar cells". PhD thesis, Swiss Federal Institute of Technology Zurich, Diss ETH Nr. 16424 (2005).

18. T.Minemoto, Y.Hashimoto, T.Satoh, T.Negami, H.Takakura & Y.Hamakawa, "Cu(In,Ga)Se2 solar cells with controlled conduction band offset of window/ Cu(In,Ga)Se2 layers". *Journal of Applied Physics* **89**, 8327-8330 (2001).

19. B.J. Stanbery, "Copper indium selenides and related materials for photovoltaic devices". *Critical Reviews in Solid State and Materials Sciences* **27**, 73-117 (2002).

20. J.Wennerberg, J.Kessler, M.Bodegard & L.Stolt, "Damp heat testing of high performance CIGS thin film solar cells". *Proceedings of the 2nd world conference on photovoltaic energy conversion, Vienna, Austria,* 1161 (1998).

21. K.Orgassa, H.W.Schock & J.H.Werner, "Alternative back contact materials for thin film Cu(In,Ga)Se-2 solar cells". *Thin Solid Films* **431**, 387-391 (2003).

22. T.Wada, N.Kohara, T.Negami, & M.Nishitani, "Chemical and structural characterization of Cu(In,Ga)Se2/ Mo interface in Cu(In,Ga)Se2 solar cells". *Japanese Journal of Applied Physics Part 2-Letters* **35**, L1253-L1256 (1996).

23. D.Rudmann, D.Bremaud, A.F.daCunha, G.Bilger, A.Strohm, M.Kaelin, H.Zogg & A.N.Tiwari, "Sodium incorporation strategies for CIGS growth at different temperatures". *Thin Solid Films* **480**, 55-60 (2005).

24. A.M.Gabor, J.Tuttle, D.S.Albin, R.Matson, A.Franz, D.Niles, M.A.Contreras, A.M.Hermann & R.Noufi, "A microstructural camparison of Cu(In,Ga)Se2 thin films grown from CuxSe and (In,Ga)2Se3 precursors". *Polycrystalline Thin Films: Structure, Texture, Properties and Applications,* 143-148 (1994).

25. L.A.Giannuzzi & F.A.Stevie, *Introduction to Focused Ion Beams*. Springer, New York (2006).

26. B.Fultz & J.M.Howe, *Transmission Electron Microscopy and Diffractometry of Materials*. Springer, New York (2002).

27. http://www.unl.edu/CMRAcfem/temoptic.htm, University of Nebraska-Lincoln.

28. S. Senapati, "Evolution of lamellar structures in Al-Ag alloys", M.S. thesis, University of Central Florida (2005).

29. D.B.Williams & C.B.Carter, *Transmission Electron Microscopy*. Plenum Press, New York (1996).

30. J.Martin, C.Fernandez-Lorenzo, J.A.Poce-Fatou & R.Alcantara, "A versatile computer-controlled high-resolution LBIC system". *Prog. Photovolt: Res. Appl.* **12**, 283-295 (2004).

31. J.F.Hiltner, "Investigation of Spatial Variations in Collection Efficiency of Solar Cells". PhD thesis, Colorado State University (2001).

32. S.A.Galloway, P.R.Edwards & K.Durose, "Characterisation of thin film CdS/CdTe solar cells using electron and optical beam induced current". *Solar Energy Materials and Solar Cells* **57**, 61-74 (1999).

33. S.A.Galloway, A.W.Brinkman, K.Durose, P.R.Wilshaw & A.J.Holland, "A study of the effects of post-deposition treatments on CdS/CdTe thin film solar cells using high resolution optical beam induced current". *Applied Physics Letters* **68**, 3725-3727 (1996).

34. R.Stengl, "High-Voltage Planar Junctions Investigated by the Obic Method". *IEEE Transactions on Electron Devices* **34**, 911-919 (1987).

35. T. Wada, N.Kohara, S.Nishiwaki & T.Negami, "Characterization of the Cu(In,Ga)Se2 /Mo interface in CIGS solar cells". *Thin Solid Films* **387**, 118-122 (2001).

36. M.Terheggen, H.Heinrich, G.Kostorz, A.Romeo, D.Baetzner, A.N.Tiwari, A.Bosio & N.Romeo, "Structural and chemical interface characterization of CdTe solar cells by transmission electron microscopy". *Thin Solid Films* **431**, 262-266 (2003).